Reconstructing 15,000 years of southern France temperatures from coupled pollen and molecular (brGDGT) markers (Canroute, Massif Central)

Léa d'Oliveira[1], Lucas Dugerdil[1,2], Guillemette Ménot[2], Allowen Evin[1], Serge D. Muller[1], Salomé
Ansanay-Alex[2], Julien Azuara[3], Colline Bonnet[1], Laurent Bremond[1], Mehmet Shah[4], Odile Peyron[1]

[1]Université de Montpellier, CNRS, IRD, EPHE, UMR 5554 ISEM, 34090, Montpellier, France
[2]Univ. Lyon, ENS de Lyon, Université Lyon 1, CNRS, UMR 5276 LGL-TPE, 69364, Lyon, France
[3]Université de Franche-Comté, CNRS, UMR 6565 Chrono-environnement, 25030, Besançon, France
[4]Université de Montpellier 3, UMR 5140 ASM, 334199, Montpellier, France

Correspondence to: Léa d'Oliveira (lea.d-oliveira@umontpellier.fr)

Abstract. Climatic changes in southern Europe during the Holocene are characterised by a strong spatial and temporal
heterogeneity whose patterns are still poorly understood, notably the presence or not of a Holocene thermal maximum (HTM;
10,000–6,000 cal. BP). The reconstructed climatic patterns also differ according to the proxies used (e.g., pollen, chironomid)
and the latitude of the data. Here, a multi-proxy approach combining pollen and lipid biomarkers (branched Glycerol Dialkyl
Glycerol Tetraethers, brGDGTs) is applied to the Canroute sedimentological sequence to reconstruct the climatic variation
over the last 15,000 years in southern Massif Central, France. This area is poorly documented in terms of vegetation and
climate. To provide reliable climate reconstructions, we have (1) performed a multi-method comparison based on transfer
functions applied to pollen (MAT, WA-PLS, BRT) and molecular biomarkers (brGDGTs), (2) investigated the role of modern
databases/calibrations in climate reconstructions. Three different calibration databases were tested for pollen data: one global
based on a Eurasian Pollen Database, and two regional databases corresponding to Mediterranean/Temperate Europe and
Temperate Europe/Scandinavian databases respectively. Nine global calibrations were tested for lipid biomarkers including
eight for soil and one for peat. The use of different modern databases highlights the importance of considering environmental
and ecological constraints when using transfer functions on pollen sequences. Pollen and brGDGT-inferred climate trends are
consistent, notably for the Lateglacial, the Early and Late Holocene. However, the reconstructions notably differ concerning
the presence of a Holocene thermal maximum with the Modern Analogue Technique (MAT) pollen-based method but not
apparent with the BRT pollen method nor brGDGT. The temperature reconstructions estimated from the two independent
pollen and lipid proxies are then compared to regional published climate signals (chironomids, pollen, molecular biomarkers)
to better derive global regional climatic patterns in South Europe. Altogether, our results from the Canroute sequence and those
already available in southern Europe reveal that for the Lateglacial and Early Holocene, the regional climate trends are coherent
between sites and proxies, supporting the reliability of their reconstructions despite some discrepancies. During the Holocene,
the temperature signal of Canroute does not indicate the clear presence of a pronounced mid-Holocene thermal maximum, but

rather stable and warmer temperature compared to Lateglacial ones and overall negative anomalies compared to modern annual temperatures.

1 Introduction

35   The Holocene Epoch (0–11,700 cal. BP) is considered to be a stable climatic period compared to the previous Lateglacial period which corresponds to the deglaciation between *ca.* 15,000 and 11,700 cal. BP and alternating phases of rapid warming and cooling (Mayewski et al., 2004). However, the Holocene nevertheless exhibits regional climate fluctuations on millennial and centennial timescales (Smith et al., 2016). In Europe, at a millennial scale, palaeoclimatological studies indicate the occurrence of a mid-Holocene optimum called the "Holocene thermal maximum" (HTM) (Liu et al., 2014) dated between

40   10,000 and 6,000 cal. BP (Renssen et al., 2012; Marcott et al., 2013; Kaufman et al., 2020; Cartapanis et al., 2022). The temperature trends during this optimum show strong latitudinal patterns which differ between regions. Marine proxies record an optimum in southern Europe and the Mediterranean region (Kaufman et al., 2020; Marriner et al., 2022), but this optimum is not clear for terrestrial proxies. The presence of the optimum is strongly dependent on latitude (Herzschuh et al., 2022). Several studies have highlighted the heterogeneous character of the Holocene climate in southern Europe, including major

45   differences according to region, as well as the proxy or seasonal parameter studied (Samartin et al., 2017; Erb et al., 2022). Pollen-based palaeoclimatic studies have highlighted the Holocene climate heterogeneity in southern Europe and suggest for the mid-Holocene similar or cooler conditions than the current ones (Cheddadi et al., 1997; Davis et al., 2003; Mauri et al., 2015; Marsicek et al., 2018; Erb et al., 2022; Herzschuh et al., 2022). However, these climate patterns are not supported by atmospheric climate model outputs, which indicate a clear warming of Europe during the Holocene (Mauri et al., 2014; Liu et

50   al., 2014; Erb et al., 2022). This highlights the need for further palaeoclimatic studies in this region, particularly in the Mediterranean basin, for which the past climate remains poorly understood (Peyron et al., 2017; Samartin et al., 2017). Terrestrial records provide especially useful information on climate change. However, terrestrial records can be influenced by environmental factors (e.g., erosion, site effect), which makes the responses of continental ecosystems to climate change difficult to interpret (Martin et al., 2020). Peatlands are powerful environmental archives, used in palaeoecology for their

55   capacity to conserve palaeoclimatic markers (Moore, 1989). The accumulation and preservation of pollen and other palaeoclimate proxies in peatlands make it possible to reconstruct quantitatively variations in climatic parameters, such as mean annual and seasonal temperatures and precipitations (Salonen et al., 2019). Peatlands are particularly rich in organic matter, conducive to the presence of lipid biomarkers such as Glycerol Dialkyl Glyceryl Tetraethers (GDGTs) (Naafs et al., 2019), whose distribution and abundance are partly governed by environmental (e.g., pH) and climatic (e.g., temperature)

60   factors, making them ideal proxies for palaeoclimatic reconstructions in the continental domain (Raberg et al., 2022). However, only few studies based on GDGTs have been carried out so far on the continental realm, mostly focusing on lacustrine environments (Sun et al., 2011; Sinninghe Damsté, 2016; Russell et al., 2018).

In recent years, quantitative reconstructions of temperature based on GDGTs were proposed both in marine and continental
ecosystems (e.g., Schouten et al., 2000, 2013; Zheng et al., 2015, 2018; Ardenghi et al., 2019; Rodrigo-Gámiz et al., 2022;

65 Dugerdil et al., 2021a, b). Transmembrane lipids, synthesised by archaea or bacteria (Weijers et al., 2009; Pearson and Ingalls,
2013), have been identified in a wide range of environments including soils, peat, and lake and marine sediments (Hopmans
et al., 2004; Weijers et al., 2006; Huguet et al., 2010; Pearson et al., 2011; Peterse et al., 2012; De Jonge et al., 2014a; Li et
al., 2016; Naafs et al., 2017a, b). Two main families of GDGTs can be distinguished: isoprenoid GDGTs (isoGDGTs) and
branched GDGTs (brGDGTs). Although the archaeal (*Thaumarchaeota*) origin of isoGDGTs has been validated, the brGDGTs

70 source remains a subject of debate and investigation (Pearson and Ingalls, 2013; Naafs et al., 2019). A relationship between
the structure of biomolecules synthesised by organisms and environmental conditions to maintain cell viability has been
demonstrated (Weijers et al., 2004). More specifically, relationships between the degree of methylation and temperature as
well as between the degree of cyclization and pH have been documented (Weijers et al., 2004, 2007). Indices and calibrations
have therefore been developed to allow the quantitative reconstruction of palaeotemperatures (Weijers et al., 2007; Peterse et

75 al., 2012; De Jonge et al., 2014a; Naafs et al., 2017a, b; Dearing Crampton-Flood et al., 2020). These calibrations were
developed from global databases that group together surface samples, for which the current climatic conditions are known,
from distinct types of substrates: soils (Peterse et al., 2012; De Jonge et al., 2014a; Naafs et al., 2017a; Dearing Crampton-
Flood et al., 2020), lake sediments (Dearing Crampton-Flood et al., 2020) and peat (Naafs et al., 2017b).

The use of brGDGTs to reconstruct annual temperatures in Europe during the Lateglacial and Holocene is still rare (e.g.,

80 Martin et al., 2020; Robles et al., 2022b; Rodrigo-Gámiz et al., 2022; Ramos-Roman et al., 2022). Due to the complexity and
number of interactions throughout the ecosystem (Birks and Birks, 2006) and the specificity of the brGDGT proxy itself, it is
advisable to use several independent proxies to obtain reliable temperature reconstructions. The general assumption is that all
proxies used to reconstruct climate changes are to some extent dependent on climatic parameters, but other factors can
influence their distribution and/or abundance (e.g., human activities, biological processes, edaphic conditions, etc.) (Sugita et

85 al., 2006; Huguet et al. 2010; Martin et al., 2020; Ponel et al., 2022). In peat, this local environmental context can be understood
through geochemical and sedimentary analyses based on X-ray fluorescence analysis (XRF) or loss on ignition (LOI), to
investigate mineral inputs and organic matter content. However, the pollen record can also be influenced by anthropogenic,
biological and environmental processes which can alter pollen production, dispersal, and preservation (Sugita et al., 2006).
Human activities, such as deforestation or agriculture, can disrupt the natural record of the vegetation-climate relationship and

90 lead to a biased quantitative reconstruction of climate parameters from pollen data (Seppä and Bennett, 2003; Birks and Seppä,
2004). The production of molecular biomarkers, such as brGDGTs, may also vary according to the production source, soil
type and vegetation (Robles et al., 2022b). Moreover, some studies report anthropogenic impacts on bacterial communities,
revealing that reconstructions based on brGDGTs can also be disrupted by human action in certain environments, such as
watersheds (Martin et al., 2019). In this sense, multi-proxy approaches are one of the best ways to estimate the reliability of

95 quantitative climate reconstructions, as it is easier to disentangle local from regional events (Ponel et al., 2022). Although some
studies compare palaeoclimatic reconstructions based on pollen and GDGTs (Martin et al., 2020; Dugerdil et al., 2021a, b;

Robles et al., 2022a, b; Ramos-Roman et al., 2022), very few have been carried out on peat sequences; with none of them concerning southwestern Europe and the Mediterranean region nor covering the entire last 15,000 years.

The aim of this study is (1) to address Holocene regional climate variability, within the context of the Holocene thermal maximum in southern Europe, from a peat sequence extracted in southern Massif Central (Canroute peatland) using a pollen-brGDGTs multi-proxy approach, (2) to contribute to palaeoclimatic reconstructions based on brGDGTs extracted from peat, which are still very little addressed in the field of biogeochemistry, and (3) to improve the reliability of the climate signal obtained from pollen data thanks to a multi-method approach (i.e., using four different methods including recent machine-learning as Boosted regression Trees) and the use of three modern pollen databases (regional to global).

2 Material and methods

1.1 Study area

The Canroute Peatland is located in the south of the Massif Central (France), in the Monts de Lacaune, Tarn department (43°38'48" N; 02°34'35" E; alt. 790 m, Fig. 1a). This soligenous *Sphagnum* peatland is supplied by several streams and small springs (Muller et al., 2018, Fig. 1b), and harbours a diversified vegetation including several species with oceanic affinity. The peatland is located at the confluence of three distinct climatic regimes: Mediterranean one from the south, oceanic one from the west and mountainous one from the north (Fig. 1a). These influences result in average annual temperatures of 9.5°C (WorldClim 2.0, Fick and Hijmans, 2017), higher summer temperatures and average annual rainfall of *ca.* 895 mm with a slightly drier summer period (Fig. 1c, Table A, CRU TS version 4.06, Harris et al., 2020).
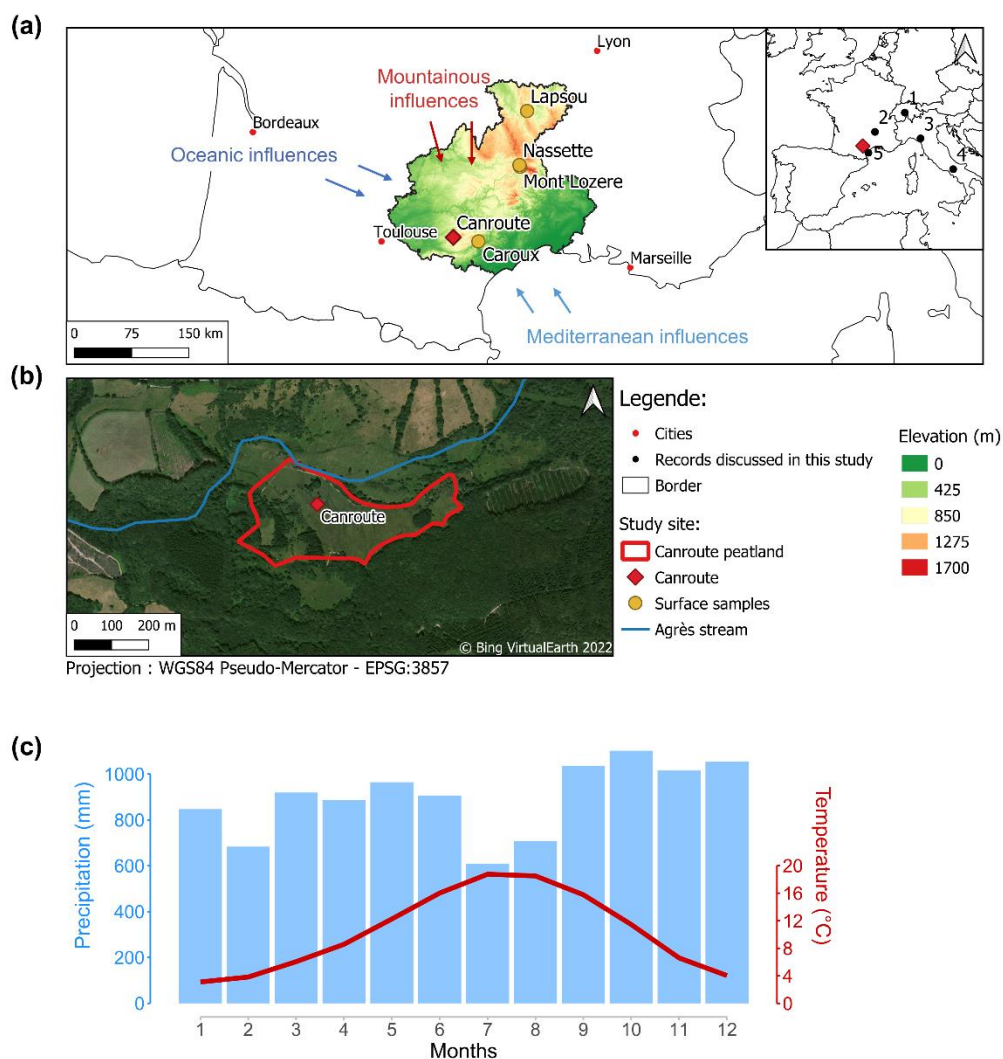
Figure 1: (a): Location and altitude of the Canroute peatland and modern surface samples (NASA JPL, 2013). Elevations of the samples departments (Aveyron, Gard, Hérault, Haute-Loire, Lozère and Tarn). The palaeoclimate records discussed in the text are represented by black dots in the inset map on the right (1: Swiss Alps, Heiri et al., 2003, 2: Lake St Front (Massif Central), Martin et al., 2020, 3: Lakes Gemini and Verdarolo (northern Apennines), Samartin et al., 2017, 4: Lake Matese (Italy), Robles, 2022a, 5: Gulf of Lion, Jalali et al., 2016). The southwestern Europe climate reconstruction provided by Davis et al. (2003) is based on numerous pollen-records (extracted from the EPD and PANGAEA databases) which are not shown for clarity. (b): Aerial view of Canroute Peatland. (c): Current annual conditions (precipitation and temperature) of Canroute (Monts de Lacaune).

2.2 Coring and sampling

The Canroute core (CAN02) extraction was carried out in 2019 using a 100 cm-long Russian corer. Two 100 cm sections were taken, spaced 20 cm apart, to cover a total depth of 169 cm. Six peat-surface samples from the Massif Central were taken to refine the selection of calibrations for the reconstruction based on brGDGTs (Fig. 1, Table A1).

2.3 Age-depth model

Radiocarbon dating of the CAN02 sequence was carried out by the Poznan Radiocarbon Laboratory (Poland) on 16 peat samples (bulk). The calibration and the age-depth model (Table 2, Fig. 2) were performed with the R language (R Core Team, 2022) and the R Studio software (RStudio Team, 2020) with the *Clam* package (Blaauw et al., 2022) using the IntCal20 calibration (Reimer et al., 2020).

2.4 Sedimentological analysis

The CAN02 sequence was analysed by energy-dispersive X-ray fluorescence (ED-XRF) spectrometry using a Delta InnovX DP4000 portable spectrometer. The analyses were conducted on bulk sediments to preserve as much material as possible for other palaeoenvironmental studies. A three-beam "soil" analytical method was used, to measure the contents of trace elements (Pb, Zn, Rb, Sr, Zr, Ba) and of Ti. The element contents of Si, K, Ca and Fe were measured using a two-beam "minerai plus" analytical mode.

The organic matter content was measured by loss on ignition (LOI) at 550°C (Ball, 1964). For this study, 16 samples of 1 cm^3 were taken every 10 cm. Each sample was weighed after drying for 12 hours at 150°C. Then, a first calcination at 550°C for 5 h was performed to estimate the organic matter content (% of dry mass) (Decorsiere et al., 2019).

2.5 GDGT analysis and indexes

2.5.1 GDGT analysis

GDGT analysis was carried out in the LGLTPE-ENS laboratory in Lyon on 75 samples of the CAN02 core with a sampling step of 2 to 4 cm, and on the 6 surface samples (Fig. 1a). Sampling was carried out using a 1 cm^3 brass cutter (about 1g) and then were freeze-dried for 24 to 72 hours. After grinding and homogenisation, the total lipid fraction was extracted twice by microwave (MARS 6 CEM) at 70° C with 10 ml of dichloromethane (DCM)/methanol (MeOH) mixture (3:1, v/v) and then filtered on SPE cartridge. 1000 ng of C46 GDGT (99 % n-hexane: 1 % isopropanol) was then added to the Total Liquid Extract (TLE) to serve as an internal standard (Huguet et al., 2006). The TLE was then separated into polar and apolar fractions on a silica column with 5 ml of hexane/DCM (1:1), and 10 ml of DCM/MeOH (1:1) respectively. The samples were then analysed in hexane/isopropanol (99.8:0.2) by high-performance liquid chromatography with mass spectrometry (HPLC-MS, Agilent 1200). Ions in Selected Ion Monitoring (SIM) are detected for mass-to-charge ratios (m/z): 744 for the internal standard C46, 1303, 1300, 1298, 1296, 1294, and 1292 for isoGDGTs and then 1050, 1048, 1046, 1036, 1034, 1032, 1022, 1020, and 1018

for brGDGTs (Hopmans et al., 2016; Davtian et al., 2021). Concentrations are expressed in mg g^{-1}$_{[sed]}$. The relative abundances of each GDGT (iso and br) are determined by the ratio of the proportion of the compound to the sum of all GDGTs. Four samples with contrasting GDGT compositions were measured and integrated five times to establish the reproducibility of the

155 analytical setup.

2.5.2 Indexes calculations

Different indices such as MBT′, MBT′$_{5Me}$, CBT, CBT$_{5Me}$, Index1, GDGT-0/Crenarcheol, and CI (Community Index) were calculated for the CAN02 sequence and surface samples (Table 1). The mean annual temperature (MAAT) was reconstructed from three types of calibrations: the linear relationship between methylation and cyclisation indices (MBT′, MBT′$_{5Me,}$ CBT)

160 (Peterse et al., 2012; De Jonge et al., 2014b; Naafs et al., 2017a) and Index1 (De Jonge et al., 2014b), multiple regression (mr and mrs) between MAAT and fractional abundances of selected brGDGTs (De Jonge et al., 2014b), and bayesian (Dearing Crampton-Flood et al., 2020). The bayesian calibration used in this study refers to the threshold-based calibration proposed by Dearing Crampton-Flood et al. (2020), which calibrates the MBT'$_{5Me}$ index to the average temperature of all months that have an average temperature above freezing.

165

Table 1: Formulae used for computation of brGDGT-indices and MAAT calibrations.

Index	Formula	Reference
CBT	$-\log 10\left(\frac{(Ib + IIb)}{(Ia + IIa)}\right)$	Weijers et al., (2007)
CBT_{5Me}	$-\log 10\left(\frac{(Ib + IIb_{5Me})}{(Ia + IIa_{5Me})}\right)$	De Jonge et al., (2014a)
MBT'_{5Me}	$\frac{(Ia + Ib + Ic)}{(I + IIa_{5Me} + IIb_{5Me} + IIc_{5Me} + IIIa_{5Me})}$	De Jonge et al., (2014a)
MBT'	$\frac{(Ia + Ib + Ic)}{(Ia + Ib + Ic + IIa + IIb + IIc + IIIa)}$	Peterse et al., (2012)
$Index1$	$\log 10\left(\frac{(Ia + Ib + Ic + IIa_{6Me} + IIa_{7Me} + IIIa_{7Me})}{(Ic + IIa_{5Me} + IIc_{5Me} + IIIa_{5Me} + IIIa_{6Me} + IIIa_{7Me})}\right)$	De Jonge et al., (2014a)
BIT	$\frac{(III_a + II_a + I_a)}{(III_a + II_a + I_a + Crenarch)}$	Hopmans et al., (2004)
III_a/II_a	$\frac{III_{a5Me}}{II_{a5Me}}$	Schouten et al., 2012
$GDGT - 0/Cren$	$\frac{GDGT - 0}{Crenarcheol}$	Blaga et al., (2009)
IR_{6Me}	$\frac{IIabc_{6Me} + IIIabc_{6Me}}{IIabc_{5Me} + IIIabc_{5Me} + IIabc_{6Me} + IIIabc_{6Me}}$	De Jonge et al., 2015

CI	$\dfrac{Ia}{Ia + IIa + IIIa}$	De Jonge et al., 2021
$MAAT_{Soil\ 5Me\ DJ.}$	$0.81 - 5.67 \times CBT + 31 \times MBT'$	Peterse et al., (2012)
$MAAT_{Soil\ MBTp\ DJ.}$	$-0.81 + 31.45 \times MBT'_{5Me}$	De Jonge et al., (2014b)
$MAAT_{Soil\ N.}$	$40.01 \times MBT'_{5Me} - 15.25$	Naafs et al., (2017b)
$MAAT_{Soil\ 5Me\ N.}$	$39.09 \times MBT'_{5Me} - 14.5$	Naafs et al., (2017b)
$MAAT_{Bog\ N.}$	$52.18 \times MBT'_{5Me} - 23.05$	Naafs et al., (2017a)
$MAAT_{Soil\ Index1\ DJ.}$	$5.05 + (14.86 \times Index1)$	De Jonge et al., (2014a)
$MAAT_{Mr\ DJ.}$	$7.17 + 17.1 \times [Ia] + 25.9 \times [Ib] + 34.4 \times [Ic]$ $- 28.6 \times [IIa_{5Me}]$	De Jonge et al., (2014b)
$MAAT_{Mrs\ DJ.}$	$5.58\ +\ 17.91 \times [Ia] + 25.9 \times [Ib] - 18.77 \times [IIa_{5Me}]$	De Jonge et al., (2014b)

2.6 Pollen analysis and reconstruction of climate parameters from pollen assemblages

2.6.1 Pollen analysis

The pollen analysis of the CAN02 sequence was carried out at the *Institut des Sciences de l'Evolution de Montpellier* (ISEM).
170 A total of 65 samples have been analysed (sampling interval of 1 cm for 159–138 cm, 2 cm for 138–128 cm, and 4 cm for 128–0 cm) and the pollen was identified and counted under an optical microscope. Pollen sums are at least 500 grains per sample and exclude spores. 148 taxa were identified, but here, a simplified pollen diagram was made to represent the vegetation variability over the last 15,000 years. The pollen data are presented as a function of age in years cal. BP. (Fig. 6)

2.6.2 Quantitative reconstruction of climate parameters

175 Various methods have been developed to quantify climatic parameters from the pollen signal (see the review of Chevalier et al., 2020) and multi-method approaches have been developed to increase the reliability of palaeoclimatic reconstructions (Peyron et al., 2005, 2011, 2013, 2017; Salonen et al., 2019; Robles et al., 2022a, b). These methods were initially developed to calibrate the relationship between modern pollen data (soils, mosses) and current climate parameters. Our multi-method approaches include (1) transfer functions, based on linear regressions (Weighted Averaging Partial-Least Squares regression)
180 between pollen taxa and climate parameters; (2) assemblage approaches, based on the analogy principle, between fossil and modern assemblages (Modern Analogue Technique), and (3) recent machine-learning technics with regression trees (Random Forest and Boosted Regression Trees) to quantify the climate parameters on the CAN02 sequence.

The Modern Analogue Technique (MAT), developed by Guiot (1990), is a method often used in palaeoclimatic reconstructions due to its simplicity of use, performance, and sensitivity. The MAT is based on measuring the degree of dissimilarity between
185 a fossil pollen assemblage and modern pollen assemblages with known environmental characteristics to draw inferences about the temporal sequences of fossil samples with unknown environmental characteristics. The WA-PLS method (ter Braak and

Juggins, 1993) is a transfer function; it assumes that the relationship between pollen proportion and climate is unimodal, where the abundance of a plant species is directly related to its environmental tolerance. WA-PLS estimates the climatic optimum of a species from calibration data by calculating the average climatological conditions in which a species occurs, weighted by the

190   abundance of that species (Chevalier et al., 2020). The other two methods (RF and BRT) have been developed more recently and are based on Machine Learning (Salonen et al., 2019). These methods use regression trees to divide pollen data by successive separations of samples according to their abundance in the pollen spectrum. Random Forest is based on the estimation and combination of many regression trees, each tree is estimated from a set of pollen samples by bootstrapping (Chevalier et al., 2020). The bootstrapping approach consists, for a database of size n, of sampling with replacement n samples

195   of the modern database to create a new database of the same size as the original database. Boosted Regression Trees differ from RF in the definition of the modern database. For RF, each sample has the same probability of being selected, for BRT the under-represented samples in the previous tree have a higher probability of being selected. This approach is called "boosting" and increases the model's performance concerning the least well-predicted elements (Salonen et al., 2019). Due to the regression tree signal variation, the BRT method's final signal is an average of 15 independent runs of the BRT algorithm.

200   For these four methods, locals and hydrophytes were not used in the reconstruction of climate parameters as they could not be strictly related to the regional climate.

The role of the modern pollen database in the reliability of climate reconstructions is also investigated here. The Eurasian Pollen Database (EAPDB, Fig. B), compiled by Peyron et al. (2013, 2017) and updated by Dugerdil et al. (2021a) was used as the first modern pollen database. In addition, two other modern pollen databases were used, originating from a sub-sampling

205   of the EAPDB database, grouping sites from the Mediterranean and Temperate Europe (MEDTEMP, Fig. B) and sites originating from Temperate Europe and Scandinavia (TEMPSCAND, Fig. B). The temperatures reconstructed from those two sub-sampled databases are compared to the temperature reconstructed from the EAPDB (Fig. 7).

Here, we reconstruct the mean annual temperature (MAAT) from the Canroute pollen record as the MAAT is the only comparable parameter between pollen and brGDGT reconstructions.

210   The reliability of pollen-inferred climate reconstruction methods was estimated by bootstrapping cross-validation by calculating the correlation coefficient values between the variables (R^2) and those of the Root Mean Square Error (RMSE) criterion.

2.7 Statistical treatments

A principal component analysis (PCA) on correlation matrix has been conducted on XRF and brGDGTs, with the *FactoMineR*

215   package (Le et al., 2008). The PCA aims to illustrate the components that explain the most variations across samples and thus permits to explore relationships between the variables. For both PCA, a k-means clustering allowed the highlight of subgroups in the data, with a chosen value of a cluster number (k) determined with a within-cluster sum of squares method. The clustering analysis has been performed with the *Factoextra* package (Kassambara and Mundt, 2017). For XRF data, due to the low

detection signal of a part of the data, a regularised imputation of the missing values has been applied, using the *missMDA*
220 (Josse and Husson, 2016) and *FactoMineR* (Le et al., 2008) packages.

Transfer functions and reliability tests were performed with the *rioja* (Juggins and Juggins, 2020), *randomForest* (Breiman,
2001) and *dismo* (Hijmans et al., 2017) packages. All analyses were performed on R Studio (RStudio Team, 2020), using the
ggplot2 (Wickham, 2016) package for plots creation and the *rioja* package (Juggins and Juggins, 2020) for the pollen diagram
with a CONISS hierarchy classification method described by Grimm (1987).

225 **3 Results**

3.1 Radiocarbon dating and age-depth model

Table 2: Dating of the 16 samples of the Canroute core with mention of their depth in cm. AMS radiocarbon-dating and calibrated
2σ age interval of the CAN02 core.

Laboratory code	Depth (cm)	AMS ^{14}C (BP)	Age (cal. BP)
Poz-129948	19–20	345 ± 30	480–310
Poz-109171	39–40	3,150 ± 35	3,450–3,260
Poz-129949	59–60	4,380 ± 35	5,040–4,860
Poz-141932	75–76	5,120 ± 40	5,980–5,750
Poz-109172	79–80	5,200 ± 35	6,160–5,900
Poz-142282	85–86	5,640 ± 40	6,490–6,310
Poz-142283	95–96	5,690 ± 40	6,620–6,360
Poz-129950	109–110	5,710 ± 35	6,620–6,400
Poz-129951	119–120	5,940 ± 40	6,880–6,670
Poz-109174	129–130	6,710 ± 30	7,660–7,510
Poz-129995	139–140	7,830 ± 50	8,970–8,450
Poz-129996	149–150	9,790 ± 50	11,310–11,110
Poz-148568	154–155	9,900 ± 50	11,600–11,200
Poz-129997	159–160	11,620 ± 60	13,590–13,340
Poz-148570	164–165	11,720 ± 60	13,750–13,460
Poz-109175	168–169	11,070 ± 50	13,100–12,840

230 The CAN02 sequence covers the Lateglacial from *ca.* 15,000 cal. BP (171 cm depth) to -80 cal. BP (surface) (Fig. 2, Table 2).
The average accumulation rate is 0.01 cm yr^{-1} between 170–113 cm, and 10 times higher between 110–85 cm (0.13 cm yr^{-1})
with a maximum value of 0.18 cm yr^{-1} at 95 cm depth (Fig. 2, shaded period). The accumulation rate drops back to initial
values between 85–15 cm. It increases again to 0.03 cm yr^{-1} from 15 to the core top.
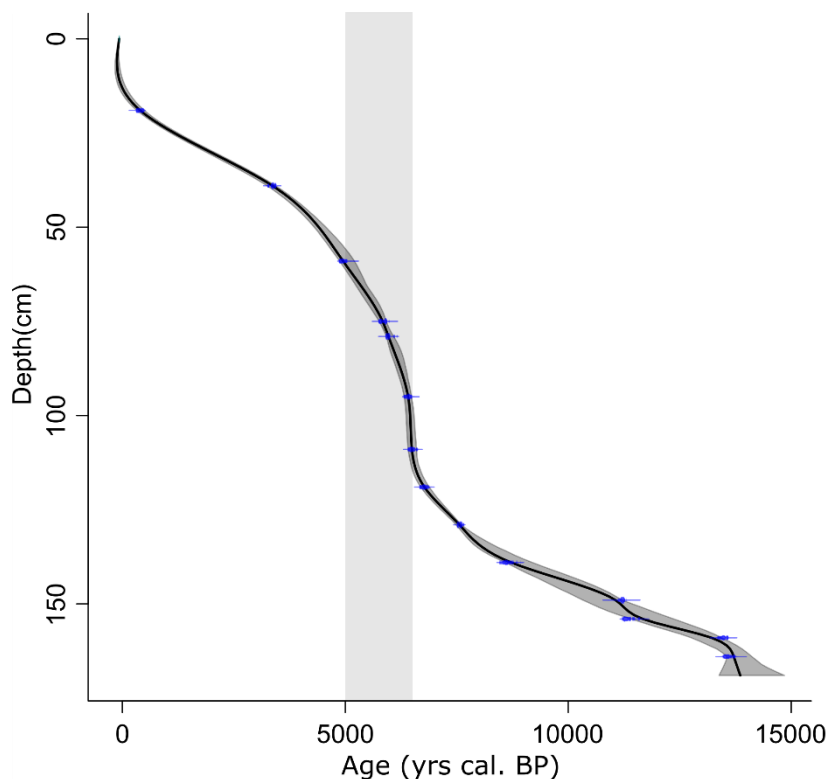
Figure 2: Age-depth model from the CAN02 sequence, built with Clam (Blaauw, 2022) on R (R Core Team, 2022). The shaded period
235 **corresponds to the interval of accumulation rate increase between 110 and 60 cm depth (6,500–5,000 cal. BP).**

3.2 Sedimentological analysis

The peat accumulation rate (PAR, Fig. 3a) ranges from 0.01 to 0.18 cm yr^{-1} with a maximum value between 6,500–6,340 cal.
BP. The two first principal components PC1$_{XRF}$ and PC2$_{XRF}$ explains 70.3 % and 9.5 % of the total elemental variation (Fig.
3e). All elements are positively correlated with PC1$_{XRF}$. The PC2$_{XRF}$ illustrates two groups of elements: elements such as Ca,
240 Ti, Si, Sr, Rb, Ba and Zr on the negative side and Pb, S, Fe, Zn and Mn elements on the positive side (Fig. 3e). The Zr element
(Fig. 3c) traces the detrital activity: the higher is the value, the higher are the lithogenic inputs (Silva-Sanchez et al., 2014).
High values of the Zr element are present from 15,000 to 9,000 cal. BP (79.2–194.0), revealing important detrital inputs,
followed by a progressive lowering of detrital inputs. From 6,500 to 3,000 cal. BP, very low values of Zr are present (0–27.9),
revealing the quasi-absence of detrital inputs. From 3,000 cal. BP onward, the values slowly increase to moderate values,
245 translating a recovery of detrital inputs. The OMC estimated from the LOI (Fig. 3d) indicates low values (under 60 %) from
15,000 to 6,600 cal. BP. After this period, the OMC increases up to 90 % from 6,600 to 3,000 cal. BP after which it decreases
to lower values (around 60 %).
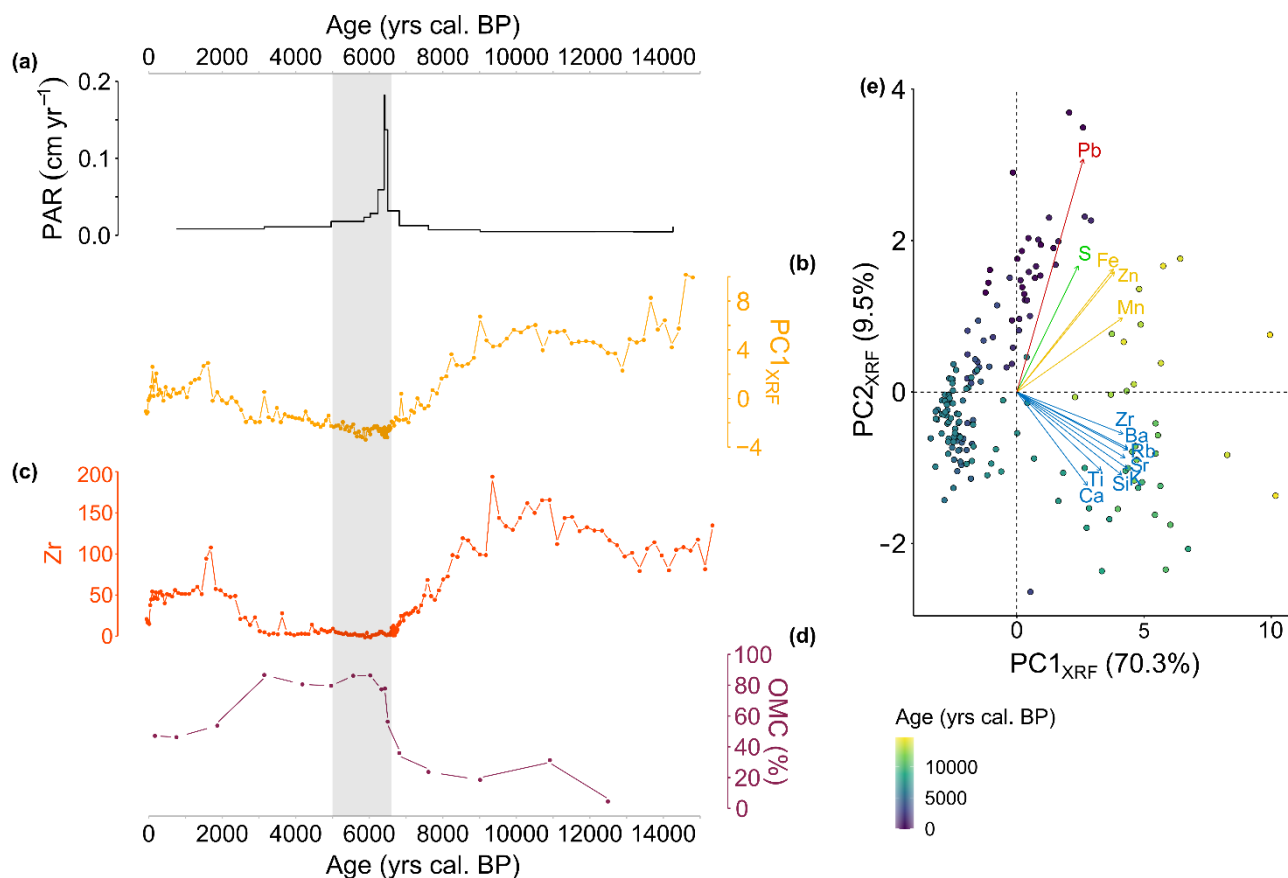
Figure 3: Geochemical data from the CAN02 sequence. (a): Peat accumulation rate (PAR) calculated from the age-depth model (cm yr⁻¹). (b): First dimension (PC1$_{XRF}$) extracted from the principal component analysis (PCA) made on the XRF data. (c) Zr element. (d): Organic matter content (OMC, %) derived from loss on ignition (LOI). (e): Principal component analysis (PCA) of the XRF signal. The principal components are grouped into four clusters. Samples are coloured according to the age gradient (yrs cal. BP). One (a) to (d) shaded period corresponds to the period between 6,600 and 5,000 cal. BP when the accumulation rate increases.

3.3 GDGTs analysis

3.3.1 Compound concentrations

In surface samples, the average concentrations of iso- and brGDGTs are 0.6 ± 0.5 mg g⁻¹$_{[sed]}$ (0.7×10^{-6}–0.4 mg g⁻¹$_{[sed]}$) and 0.8 ± 0.6 mg g⁻¹$_{[sed]}$ (0.9×10^{-6}–2.2 mg g⁻¹$_{[sed]}$), respectively. The CAN02 core samples have higher average concentrations of iso- and brGDGTs than the surface samples: 2.1 ± 2.0 mg g⁻¹$_{[sed]}$ (53.0–1.5 mg g⁻¹$_{[sed]}$) and 2.4 ± 2.0 mg g⁻¹$_{[sed]}$ (143.6–29.7 mg g⁻¹$_{[sed]}$), respectively.

3.3.2 Relative abundances

260 Average analytical errors are calculated from the averaged standard deviations of replicate measurements for br- and isoGDGTs (sd = 2 and 4 % respectively, n = 75). Br- are predominant over iso-GDGTs in the 7 surface samples (including CAN0) (average abundance of 92 % and 7 % respectively, Fig. C). IsoGDGTs of surface samples are dominated by GDGT-0 (between 47 % and 96 %, Fig. 4a). BrGDGT relative abundances in surface samples show the dominance of tetramethylated (Ia) and pentamethylated (IIa) (36 % and 37 % respectively, Fig. 4b). For CAN02 downcore samples, average relative

265 abundances of iso- and brGDGTs show mean values of 12 % and 88 % respectively (Fig. C). Downcore samples are also dominated by GDGT-0 (isoGDGTs) and tetramethylated and pentamethylated (brGDGTs) (Fig. 4a, b).
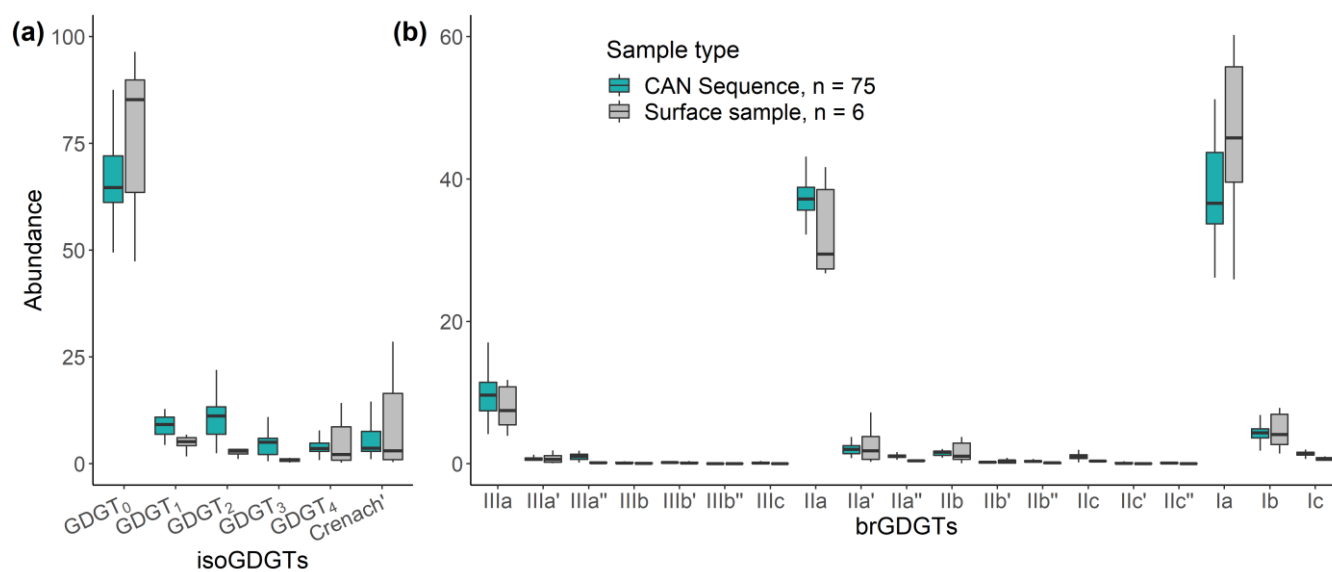
Figure 4: GDGT results: Fractional abundances (%) of (a) isoGDGT and (b) brGDGT compounds for the CAN02 sequence (n = 75, blue) and surface samples (n = 6, grey).

Penta- and hexamethylated brGDGTs show similar trends: a decrease between 15,000–6,600 cal. BP followed by an increase

270 between 6,600–6,100 cal. BP and a further decrease between 6,100 and -80 cal. BP (Fig. 5a). Tetramethylated brGDGTs show the opposite trend: an increase between 13,800–6,600, followed by a sharp decrease between 6,600–6,300 cal. BP and then a gradual increase between 6,300 and -80 cal. BP. Pentamethylated brGDGTs dominate between 15,000–5,000 cal. BP, whereas tetramethylated brGDGTs dominate from 5,000 cal. BP onwards. The CBT_{5Me} index varies between 0.92 and 1.42 (sd = 0.05; n = 75, Fig. 5b), it is constant between 15,000–6,600 cal. BP then a slight increase can be observed between 6,600–6,300 cal.

275 BP before a more important increase of the CBT_{5Me} between 4,700–3,300 cal. BP. The MBT'_{5Me} index varies between 0.32 and 0.55 (sd = 0.01; n = 75) and shows a slightly increasing trend over time (Fig. 5c), with two periods of rapid decrease between 6,600–6,400 cal. BP and between 290 and -80 cal. BP and two well-differentiated periods: 15,000–6,600 and 5,000–290 cal. BP. The Community Index (CI) values range from 0.30 to 0.55 and are lower than 0.65 throughout the record (Fig.

5d). Period from 15,000 to 5,000 cal. BP is associated with mean CI values of 0.38, whereas the period from 5,000 to -80 cal.

280   BP is associated with higher mean CI values of 0.49.

The PCA performed on brGDGT relative abundances show that PC1 and PC2 explain over 60 % of the variance (PC1$_{brGDGTs}$ 49.9 %, PC2$_{brGDGTs}$ 11.7 %) (Fig. Dd, e). The lower half of the sequence (15,000–5,000 to 8,5000 cal. BP) is positively correlated with all brGDGTs, while the upper half (from 5,000 cal. BP onward) is negatively correlated with them. As a result, the GDGT-0/Cren ratio, which varies from 4.4 to 84.8, decreases through time and illustrates the diminution of GDGT-0 in

285   favour of Crenarcheol (Fig. Da).
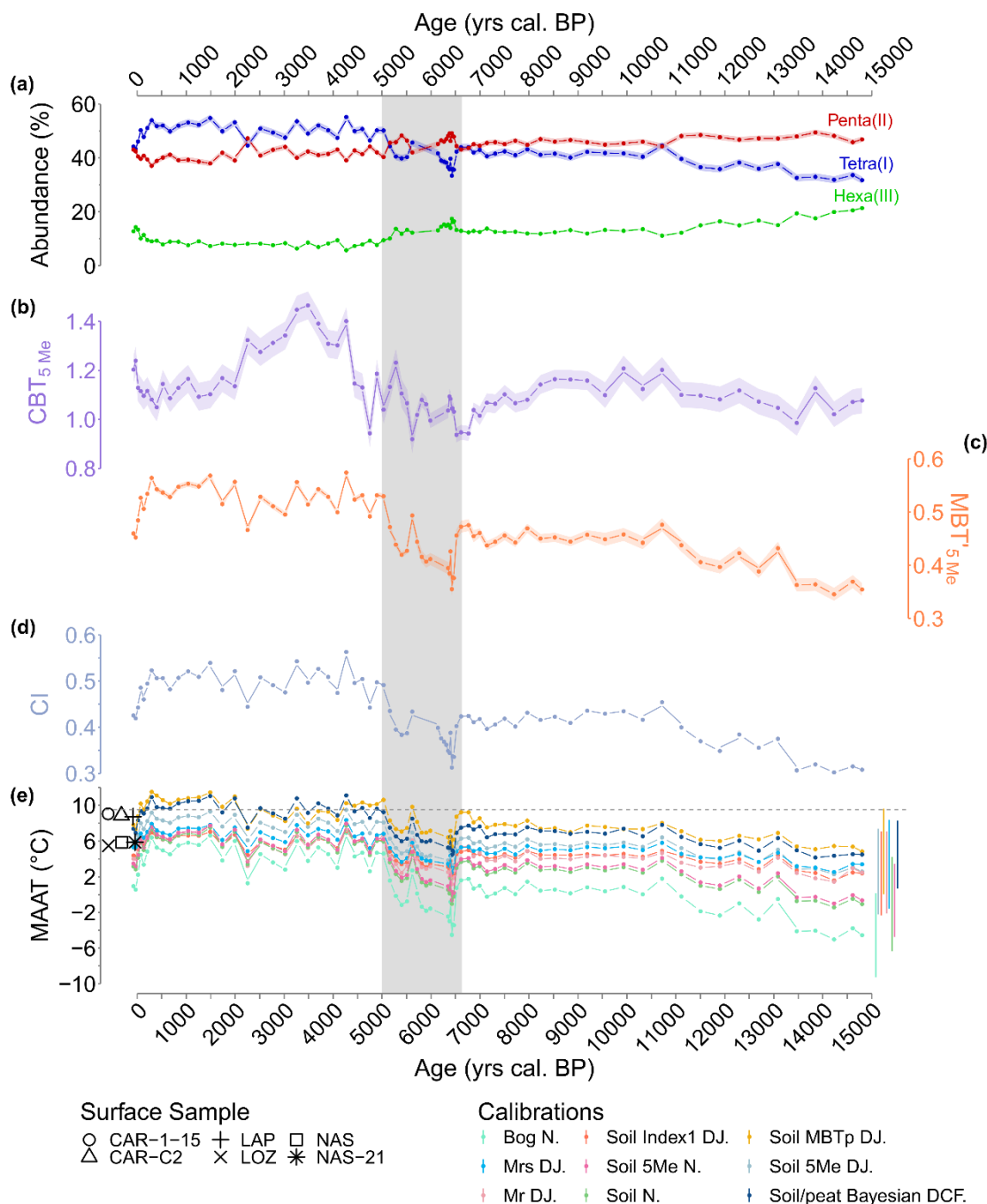
Figure 5: (a): Relative abundances of tetra-, penta- and hexamethylated brGDGTs in the CAN02 sequence. (b): Index of the degree of cyclisation (CBT$_{5Me}$). (c): Index of the degree of methylation (MBT'$_{5Me}$). (d): Bacterial Community Index (CI) through time. (e): Annual mean temperature (MAAT) reconstructions based on global calibrations of De Jonge et al., (2014a) (Soil Index1 DJ., Soil MBTp DJ., Mr DJ., Soil 5Me DJ.), Naafs et al., (2017a) (Bog N., Soil 5Me N., Soil N.) and Dearing Crampton-Flood et al., (2020)
290 **(Soil Bayesian DCF.). Calibration errors are represented by the lateral lines on the right side. Shaded period highlights the significant decrease in abundance of tetramethylated brGDGTs and a shift in accumulation rate. Symbols: modern MAATs of surface samples. Black dashed line: current MAAAT at Canroute.**

3.3.3 Palaeotemperature reconstruction

All calibrations show similar trends during the Holocene, i.e. (1) cold conditions between 15,000–11,000 cal. BP, followed by
295 (2) warmer conditions until 6,600 cal. BP (Fig. 5c). This stable period ends with (3) a drop in temperature between 6,600–
5,000 cal. BP and is followed by (4) a new warming until 300 cal. BP, before (5) a new last drop in temperature (Fig. 5c).
Despite similar and synchronous trends, the absolute values of temperature are different between calibrations. From the
Lateglacial to the present, the peat calibration shows the lowest MAAT values, ranging from -5.0 to 6.9°C (sd = 0.5°C, n =
75) whereas multiple regressions (mr and mrs), Index1, MBT', MBT'$_{5Me}$ and bayesian calibrations are associated with higher
300 MAATs values ranging from -1.43 to 11.51°C (sd = 0.3°C, n = 75). Among all calibrations, the multiple regressions, the
bayesian and the one based on Index1 shows the lowest variations (respectively 7.2, 6.9 and 5.5°C) compared to the peat
calibrations and those based on methylation indexes (respectively 11.5 and 12.9°C).

3.4 Pollen analysis

The Zone 1 (from 15,000 to *ca.* 11,700 cal. BP) of the pollen diagram (Fig. 6) is dominated by herbaceous taxa of steppe
305 (*Artemisia*, Amaranthaceae, Poaceae), peatland (Cyperaceae up to 50 %) and megaphorbia (*Filipendula, Ranunculus, Succisa
pratensis*), but contains some occurrences (mostly of long-distance origin) of *Betula, Corylus avellana, Pinus sylvestris*-type
and *Quercus pubescens*-type. At the end of this period, the arboreal pollen represents *ca.* 45 % of the pollen sum, indicating
the gradual replacement of the steppe vegetation by forests.

The Zone 2 (from 11,700 to 6,600 cal. BP) is dominated by *Corylus avellana* (up to 60 %), and to a lesser extent by *Quercus
310 pubescens*-type (< 30 %) that progressively increases. During this period, the record of steppe taxa decreases, but hydrophytes
are still present.

The Zone 3 (from 6,600 to *ca.* 4,500 cal. BP) is marked by an increase in *Quercus pubescens*-type and *Tilia* at the expense of
Corylus avellana. This period is also marked by the decrease in megaphorbia taxa and by the record of Poaceae, *Calluna
vulgaris* and *Sphagnum*.

315 Finally, the Zone 4 (from *ca.* 4,500 to -80 cal. BP) is characterised by the mesophilous *Abies alba* and *Fagus sylvatica*, and
the hydrophyte *Alnus glutinosa*-type. *Corylus avellana* and *Quercus pubescens*-type continue to decrease, while *Tilia* is only
slightly recorded.
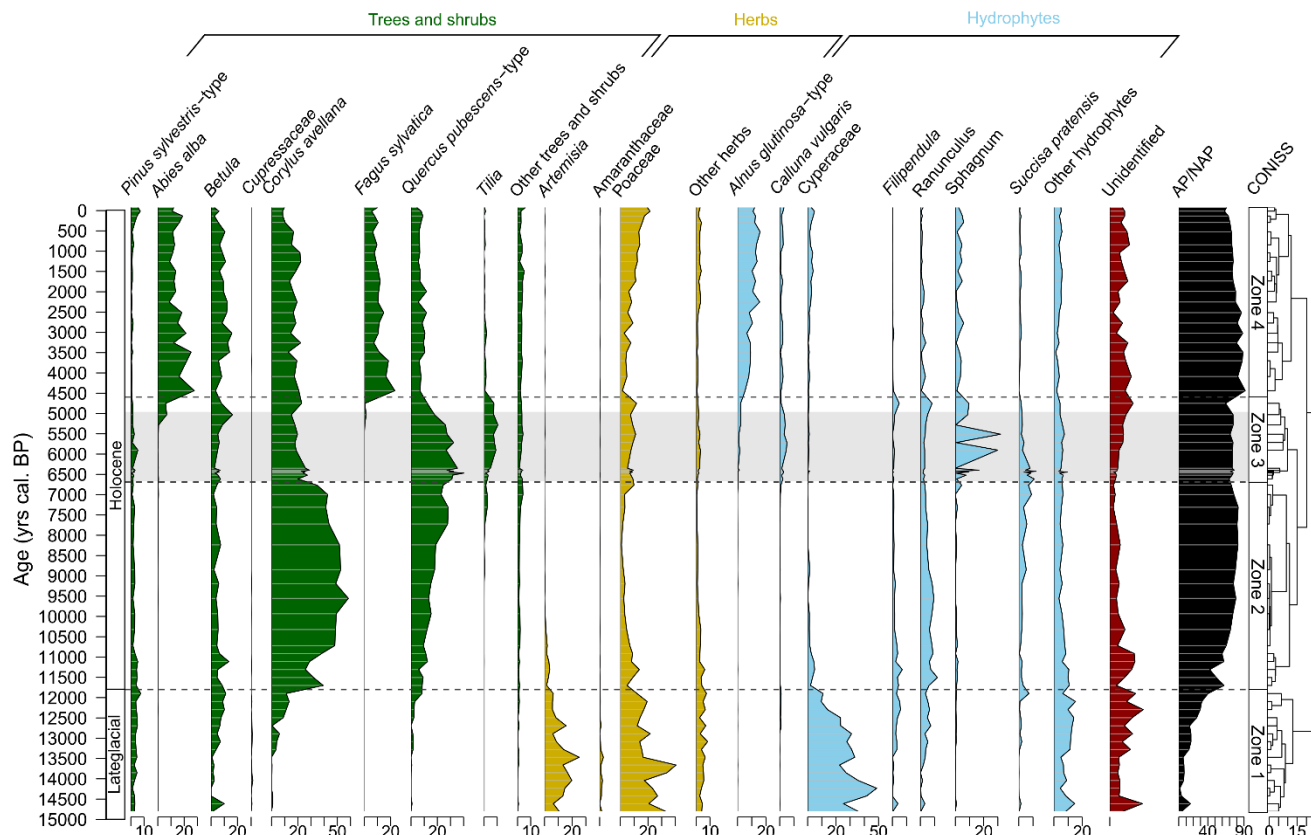
Figure 6: Simplified pollen diagram of the CAN02 sequence grouping selected tree taxa (green), herbaceous taxa (yellow), hydrophytes (blue) and AP/NAP ratio (black). Percentages were calculated on pollen sums excluding spores. The black dashed lines delineate 4 zones based on CONISS. The shaded period highlights the period of significant decrease in tetramethylated brGDGTs abundance (6,600–5,000 cal. BP) and a shift in accumulation rate.

3.5 Pollen-inferred mean annual temperature

To provide reliable climate reconstruction, we applied to the Canroute pollen assemblages a multi-method approach tested with three different modern pollen databases. The results based on the global EAPDB and regional TEMPSCAND databases indicate broadly the same temperature trends, but with smaller amplitudes for the TEMPSCAND calibration. The MEDTEMP regional calibration shows opposite trends compared to the other two databases, particularly during the Lateglacial (Fig. 7). The EAPDB and TEMPSCAND databases are associated to higher values of R^2 than the MEDTEMP ones (Table 3).

For the EAPDB and TEMPSCAND, three of the methods (MAT, WA-PLS and BRT) show a similar climatic signal (Fig. 7a, b, d) characterised by (1) cold temperatures during the Lateglacial, followed by (2) a warming through the Early Holocene, resulting in a thermic optimum accentuated depending on the methods used, then (3) a sudden cooling around 6,000 cal. BP, again followed by (4) a slight warming for 5,000 cal. BP onward. Cold conditions (MAAT around 2.3 to 8.7°C) are evidenced from 15,000 to 11,700 cal. BP. The first warming occurs between 11,700 and 6,000 cal. BP. The WA-PLS (and the MAT)

indicate high values for this thermal optimum (Fig. 7a, b). While the BRT method indicates a warming of 1.5° C between 12,000 and 6,500 cal. BP (Fig. 7d). The duration of the cooling observed around 7,000–6,500 cal. BP is method dependent.

335   The cooling reconstructed with the MAT and WA-PLS is progressive with a variation in the MAAT of -2.1 and -4.5° C respectively and is shorter for the MAT than for the WA-PLS (Fig. 7a, b). The BRT indicates a slight cooling between 6,400 and 4,700 cal. BP, less marked than for the other two methods, with a variation of -0.9° C (Fig. 7d). The last period is characterised by a slight warming trend particularly marked for the BRT and WAPLS methods with an increase of +2.4 and +2.6° C respectively. The MAT indicate a warming of 1.9 (Fig. 7c). BRT, MAT and WA-PLS are the three methods with the

340   largest temperature amplitudes. The RF shows a much less contrasting climate signal over time (3.4° C variations between 15,000 cal. BP and present, Fig. 7c), a climate pattern that is different than from the results obtained with the MAT, WA-PLS and BRT methods. Contrary to the EAPDB and TEMPSCAND calibrations, the MEDTEMP shows a warm Lateglacial and the absence of the thermic optimum for the four methods (Fig. 7).

The BRT method shows higher values of R^2 (Table 3, $R^2 = 0.92$; RMSE = 1.30), and the RF method shows lower values of R^2

345   = 0.70 (RMSE = 1.83).
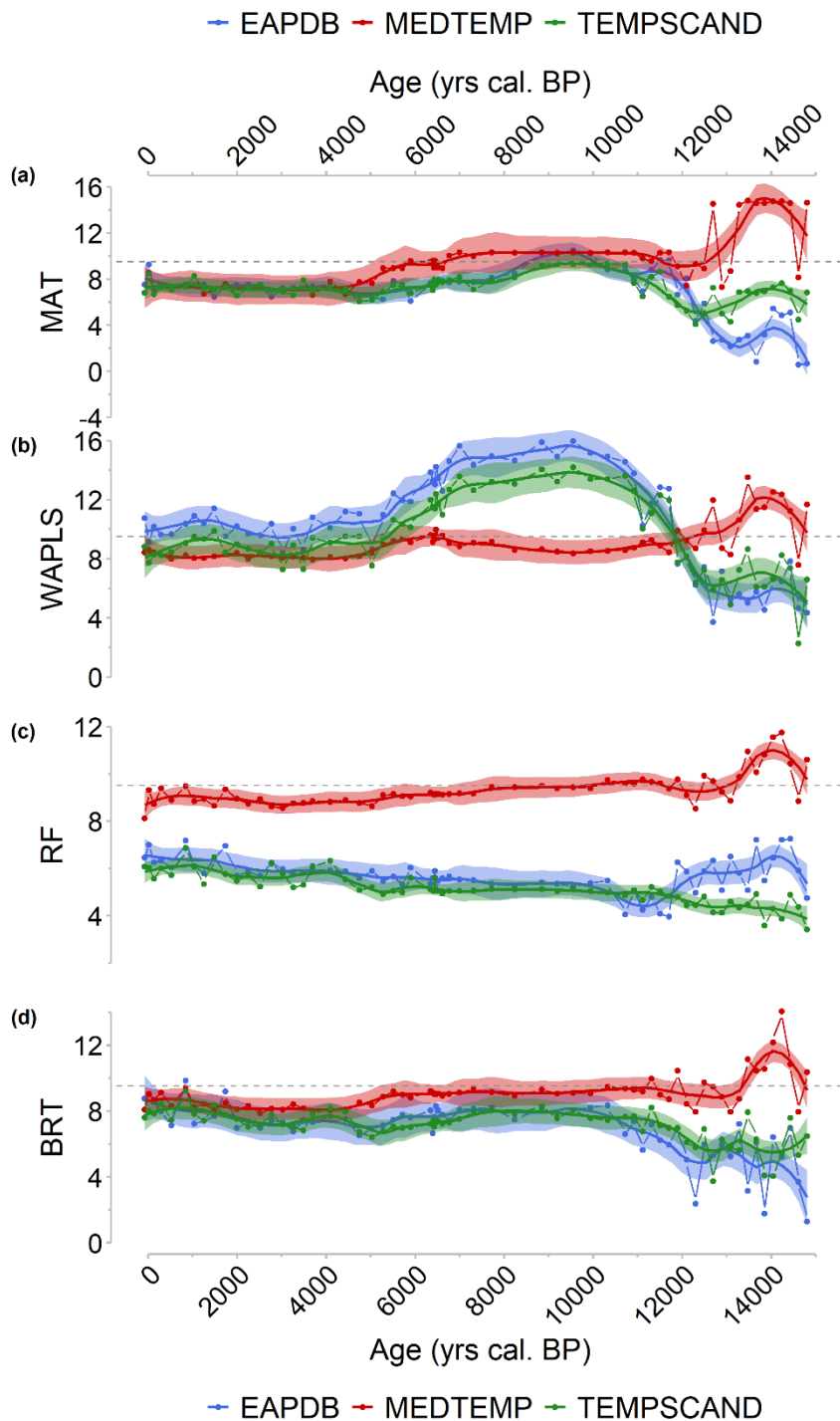
Figure 7: Climate signal from the three calibration sets EAPDB (blue), MEDTEMP (red) and TEMPSCAND (green) for the MAT (a), the WA-PLS (b), the RF (c) and the BRT (d) methods. Black dashes: current MAAT at Canroute.

Table 3: Performance results of the MAT, WA-PLS, BRT and RF methods applied to three different modern pollen databases: the modern Eurasian (EAPDB), Temperate-Scandinavian (TEMPSCAND) and Mediterranean-Temperate (MEDTEMP) databases for mean annual air temperature (MAAT° C). k is the number of parameters used in the methods (e.g., number of analogues for the MAT method or the number of PLS components for the WA-PLS method). The best k corresponds to the number of parameters that infer the best R^2 and calibration error (RMSE) values. The chosen k corresponds to the lowest number of parameters associated with the best R^2 and RMSE values. In bold: Selected database and methods associated with their respective R^2 and calibration error (RMSE) values.

Database	Methods	Best k R^2	Best k RMSE	Chosen k	Chosen R^2	Chosen RMSE
EAPDB	MAT	4	6	4	0.87	3.09
	WA-PLS	3	3	3	0.71	4.11
	BRT	-	-	-	0.92	2.55
	RF	-	-	-	0.68	4.26
TEMPSCAND	**MAT**	3	6	3	**0.87**	**1.41**
	WA-PLS	3	3	3	0.60	2.14
	BRT	-	-	-	**0.92**	**1.30**
	RF	-	-	-	0.70	1.83
MEDTEMP	MAT	3	9	3	0.86	2.14
	WA-PLS	3	3	3	0.67	2.92
	BRT	-	-	-	0.91	2.02
	RF	-	-	-	0.74	2.45

4. Discussion

4.1 Past vegetation, peat accumulation and detrital activity

The Lateglacial steppe environment, dominated by *Artemisia*, Poaceae and to a lesser extent Amaranthaceae (including the ex-Chenopodiaceae), reveals cold and dry conditions. However, the record of Cupressaceae (only represented by *Juniperus* at that time) and especially *Betula* reveals the first afforestation dynamics supported by the slight warming of the Bølling-Allerød period. The end of the Lateglacial is characterised by the early expansion of temperate deciduous forests of *Corylus avellana* and *Quercus pubescens*-type, surprisingly contemporaneous with the Younger Dryas cooling event (12,900–11,700 cal. BP; e.g. Broecker et al., 2010; Denton et al., 2010). Although the whole Younger Dryas is well recorded in northern regions (e.g., Duprat-Oualid et al., 2022), only the onset of the period is marked at Canroute by a peak of *Artemisia* and Amaranthaceae, and a punctual decrease in both *Corylus avellana* and *Quercus pubescens*-type.

The beginning of the Holocene is marked by a strong dominance of *Corylus avellana* that constituted woodland, whose open character allowed the strong detrital activity revealed by XRF until 9,000 cal. BP. After this date, the progressive decrease in detrital activity may be attributed to the slow expansion of deciduous oaks, which replaced hazelnut woodland across southern

France. However, the slower establishment of dense deciduous forests compared to the southern Alps (de Beaulieu, 1977; de Beaulieu and Reille, 1983) suggests the influence of unfavourable climate conditions which slowed oak progression.

370   The emergence of a dense mature oak forest is attested between 6,600 and 5,000 cal. BP by both the maximal pollen record of *Quercus pubescens*-type and *Tilia* (Fig. 6), and the decrease in mineral input (Fig. 3b, c) that reveals the reduced detrital activity. Such a vegetation change occurring on the surrounding slopes is likely to have triggered hydrological changes within the studied wetland, which effectively experienced several contemporaneous changes: an abrupt acceleration of peat accumulation (Fig. 3a), an increase in organic matter content (from less than 40 % to more than 80 %; Fig. 3d; Joosten 2015)

375   and a replacement of the previous megaphorbia by a bog-type peatland dominated by *Calluna vulgaris* and *Sphagnum* (Fig. 6). These changes are consistent with a loss of water runoff on the wetland surface, the result of either a reduced water supply resulting from a change in the river system or the natural rise of peatland surface that progressively isolated peat-forming vegetation from groundwater. Finally, change affecting both the local hydrophytic vegetation and the surrounding landscape occurs at *ca.* 4,500 cal. BP when the open peatland system is replaced by an alder swamp dominated by *A. glutinosa* (the only

380   *Alnus* species present in the Massif Central), and the deciduous oak forest declines in favour of a mixed fir-beech forest. While this change could be interpreted as an environmental shift towards "mountainous" conditions, the contemporaneous pollen record of *Plantago* (not seen) and the late-Neolithic date (Miras et al., 2004) suggest anthropogenic impact, which likely destabilised the competitive equilibrium in favour of the mixed forest onset.

4.2 Temperature signal from brGDGTs

385   ### 4.2.1 Consistency of brGDGTs relative abundances with peat and soils databases

The Canroute fossil samples and the surface samples from Massif Central are consistent with the global peat and soil databases that are globally dominated by tetra- and pentamethylated brGDGTs (Fig. 8a, Yang et al., 2014; Naafs et al., 2017a, b; Dearing Crampton-Flood et al., 2020). The use of both types of calibrations (peat and soil) therefore appears to be consistent with the brGDGT assemblages observed in the CAN02 sequence.
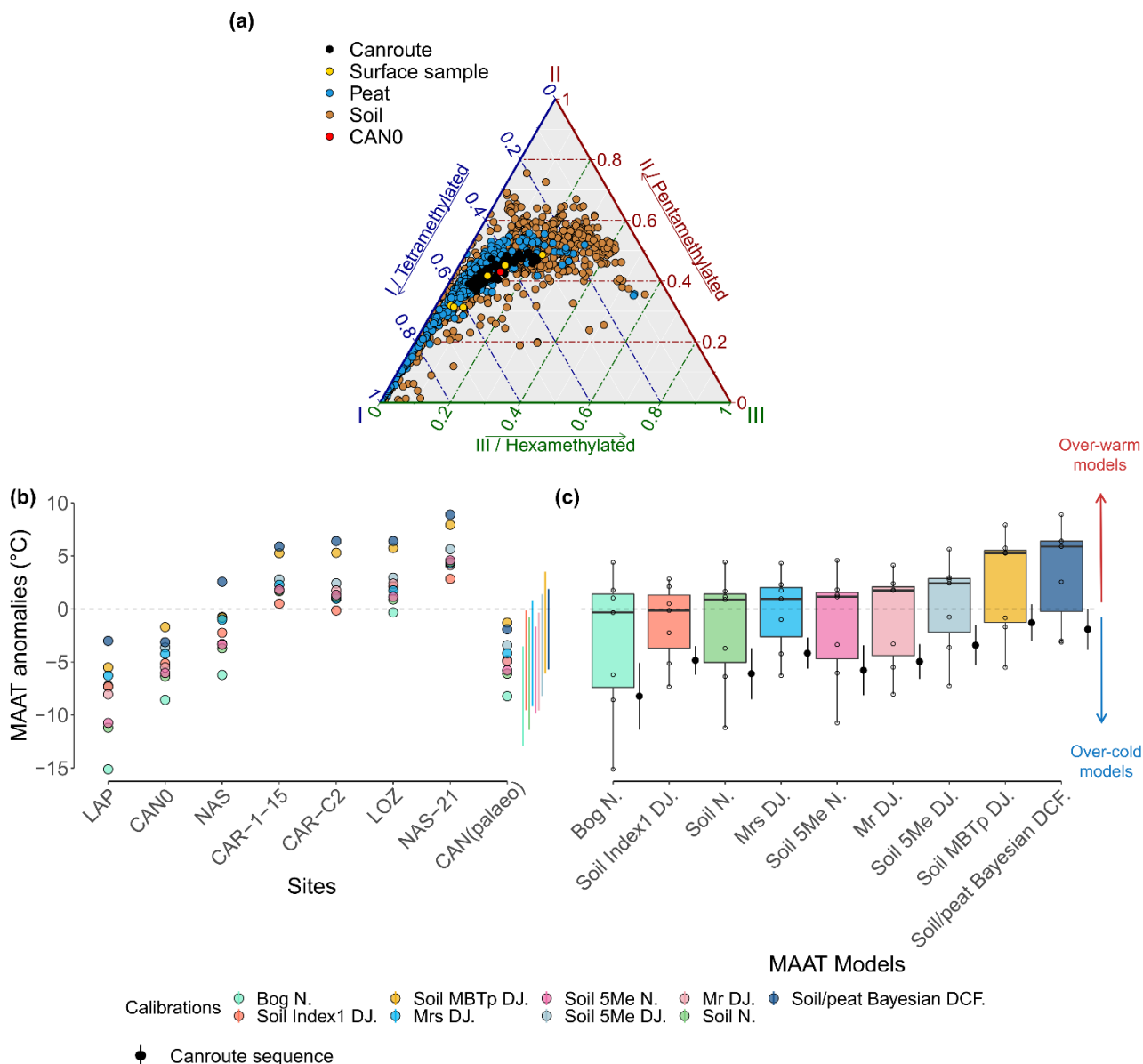
Figure 8: (a) Ternary plot of fractional abundances of tetra-, penta- and hexamethylated brGDTs for CAN02 core samples (in black)
390 **and Massif Central surface samples (in yellow and red); and for global peat (Naafs et al., 2017b, in blue) and soil databases (Yang**
et al., 2014; Naafs et al., 2017a; Dearing Crampton-Flood et al., 2020, in brown). (b, c): Testing of soil and peat calibrations on
surface samples and CAN02 core samples. (b): Reconstructed MAAT from each calibration expressed as anomalies with respect to
the mean annual temperatures measured at the sites. The standard deviation of each calibration applied to the CAN02 sequence
395 **(palaeo) is represented by the lateral lines on the right side. (c): Boxplot representing the results of the calibrations applied to the**
surface samples (*n* = 6). Black points with error bars next to each calibration correspond to temperature anomalies of CAN02 core
samples.

4.2.2 Selection of the relevant brGDGT-calibrations

The brGDGT relative abundances in the surface samples of Nassette (NAS), Lapsou (LAP) and Canroute (CAN0) are close to
400 that of the Canroute (CAN02) sequence (Fig. C). For these three samples, the Bayesian calibration (Soil Bayesian DCF,
Dearing Crampton-Flood et al., 2020), the ones based on MBT′ (Soil MBTp DJ.), Index1 (Soil Index1 DJ.) and multi-
regression (Mrs DJ.) (De Jonge et al., 2014a) show more reliable reconstructed MAAT anomalies (Fig. 8b). For the samples
from the Caroux site (CAR-1-15 and CAR-C2), which is also a soligenous peatland and is geographically the closest site to
Canroute (Fig. 1a), the calibrations based on Index1, and multi-regression appear to be the most reliable (Fig. 8b). For the
405 Canroute surface sample (CAN0), the calibration based on the MBT′ (Soil MBTp DJ.) and the Bayesian calibration (Soil
Bayesian DCF.) provides temperature values closer to the present temperatures (Fig. 8b). Soil calibrations based on Index1,
MBT′, multi-regression and Bayesian calibration produced the most suitable MAATs: both the Index1 and the multi-regression
calibrations show a good estimate of the current MAAT, with a low scatter and a current MAAT close to the observed climatic
conditions (Fig. 8c). When applied to the whole sequence (CAN02), these two calibrations (Index 1 and Mrs) have the lowest
410 standard deviations (respectively sd = 1.4°C and 1.5°C; n = 75, Fig. 8c). Regarding the Bayesian and MBT′ calibrations, they
show a less reliable estimate of the current MAAT and have close standard deviation when applied to the CAN02 sequence
(sd = 1.9°C; n = 75, Fig. 8c). However, the Bayesian calibration is associated with a lower error than the MBT′ based one
(RMSE = 3.8°C and 4.8°C respectively, Fig. 8b). Ultimately, among the 9 calibrations tested, 3 of them (Bayesian, Index1 and
multi-regression) are retained for the interpretation of the climate trend, due to the low RMSE of the Bayesian calibration and
415 the low standard deviations of Index1 and multi-regression calibrations reconstruction when applied to the CAN02 sequence.

4.2.3 Interpretation of the climate signal

Cold conditions from 15,000 to 11,000 yrs BP give way to gradually increasing temperatures before dropping from 300 cal.
BP onward. Between 6,600 and 5,000 cal. BP, however, we reconstruct a strong cooling that is not generally observed in the
region (Fig. 5e, shaded area). No clear environmental change is highlighted by the brGDGT indices such as BIT and III$_a$/II$_a$,
420 which only vary from 0.97 to 0.99 and from 0.12 to 0.46 respectively. Although the CI value does not cross the 0.65 threshold
established by De Jonge et al. (2021), a marked decrease in value indicates changes in the bacterial community producers of
brGDGTs in the sequence (Fig. 5c) that might prevent the interpretation of temperatures between 6,600 cal. BP and 5,000 cal.
BP.

According to various studies in peatlands, communities of brGDGT-producing bacteria are controlled by local hydrological
425 conditions (Rao et al., 2022) and vegetation composition (Xiong et al., 2016), whose changes are thus likely to affect
temperature reconstructions (De Jonge et al., 2019). The GDGT-0/Cren ratio is used to investigate the presence of
methanogenic archaea that flourish in anoxic conditions in the sediments (Blaga et al., 2009). Crenarcheol is also an indicator
of the water-table level, which refers to the limits between the acrotelm and catotelm in peatlands, and therefore is an indicator
of anaerobic conditions (Yang et al. 2019). In the CAN02 sequence, the abundance of GDGT-0 decreases in favour of

Crenarcheol through time (Fig. Da). This points to less anoxic conditions, indicating that the Canroute water-table level lowers over time, making the peatland surface drier. This correlates well with other proxies such as geochemical and pollen data that evidences a hydroseral succession from a water-demanding megaphorbia to peatland and alder-swamp plant communities. Dearing Crampton-Flood et al. (2020) used two indicators of the presence or absence of climate seasonality, in terms of precipitation and temperature, to investigate a possible bias in the production of brGDGT compounds. Seasonality of Precipitation (SoP) is based on the difference between MAP_{max} and MAP, a low SoP value being indicative of a relatively constant MAP through the year. The SoP index can aid in interpreting whether a region presents a potential production bias due to variability in timing of precipitation (Dearing Crampton-Flood et al., 2020). Canroute is associated with a low SoP value (24.4) and therefore does not show a heterogenous precipitation pattern, which can create a bias in the production of brGDGTs. Temperature Seasonality (TS) is quantified as the difference between $MAAT_{max}$ and $MAAT_{min}$. A region associated with a TS value over 20 is considered to have high-temperature seasonality, which biases the proxy toward summer temperatures (Dearing Crampton-Flood et al., 2020). At Canroute, the TS value is 16.6 which indicates a low-temperature seasonality, without bias.

Consequently, the climate signal reconstructed by brGDGTs does not seem to be drastically impacted by the changing environmental context before and after the 6,600–5,000 cal. BP period. However, during the 6,600–5,000 cal. BP period, the shift from a running water-demanding vegetation to a less-demanding one (Fig. 6) seems to induce a shift in brGDGT indexes. The temperature values reconstructed for this period (Fig. 5e, shaded area) thus must be interpreted with caution.

4.3 Climate signal from pollen

Different studies underline the importance of the modern pollen database used for the reconstruction of climate parameters (Turner et al., 2021) and point out the advantage of regional calibration databases (Dugerdil et al., 2021a, b). The calibrations performed with the Eurasian pollen database (EAPDB) and regional Temperate and Scandinavian pollen database (TEMPSCAND) broadly indicate similar temperature trends at Canroute, while the Mediterranean and Temperate pollen database (MEDTEMP) calibration shows opposite trends compared to the other two calibrations (Fig. 7). These discrepancies can be explained by the dominance, at this period, of taxa such as *Artemisia*, Amaranthaceae and Poaceae (Fig. 6), able to constitute physiognomically and floristically similar arid steppes, both in the southern Mediterranean and Irano-Turanian warm context (e.g., Le Houérou, 2001) and in the north-eastern Eurasian cold context (e.g., Yurtsev, 1982). From 11,700 cal. BP onwards, the methods performed on the three databases show similar trends but with different amplitudes. Signals obtained with the EAPDB and TEMPSCAND databases are particularly close, especially for the MAT and BRT methods (Fig. 7a,d). However, the absence of Mediterranean taxa in the pollen sequence (Fig. 6), as well as the poor R^2 and RMSE values (Table 3), allow the MEDTEMP calibration to be dismissed as a reliable calibration for MAAT quantification.

Among the four methods, RF and WA-PLS appear as the least reliable (low R^2 and high RMSE, Table 3), so the MAATs reconstructed by these two methods will not be considered in the following discussion. For the MAT and BRT methods, the TEMPSCAND database calibration seems to produce a signal as reliable as the one produced with the EAPDB calibration set

(close R² and RMSE values, Table 3). The TEMPSCAND calibration produces a particularly close signal between the two methods and possess better R² and RMSE values, supporting the reliability of the reconstructions based on this calibration
465 database, and will be considered in the following discussion (Fig. 9).

MAT and BRT are two methods based on different mathematical and ecological concepts (Chevalier et al., 2020), so their similar reconstructed trend supports the reliability of the methods and calibrations. However, the MAT shows a larger temperature range and in particular a slight thermal optimum in the Early Holocene, between 11,700–8,000 cal. BP (Fig. 7a). A similar pattern, although marked by more pronounced positive anomalies, is shown by Martin et al. (2020) for Lake St Front
470 where high percentages of *Corylus* (< 55 %) are also recorded. Such a high proportion of *Corylus* does not exist in the modern pollen database assemblages. The highest proportion (25–35 %) is associated with sites located in Italy, Ireland, and Albania, explaining the bias in the signal towards higher temperatures for the EAPDB- and TEMPSCAND-based calibrations. In the CAN02 pollen sequence, the Early Holocene is also characterised by high *Corylus* percentages (up to 60 %, Fig. 6), which could explain the large temperature variation between the Lateglacial and Early Holocene proposed by the MAT, the only
475 method based on the similarity of present-day/fossil assemblages. For the 10,700–6,600 cal. BP period, it can be suggested that the MAT method is less efficient than the BRT one, because Early-Holocene hazelnut woodland have no modern analogue. Nevertheless, both the MAT and BRT methods calibrated on the TEMPSCAND database can be retained in the following discussion because of the good reliability of their reconstructions.

4.4 Annual temperatures in the northern Mediterranean basin since the Lateglacial

480 #### 4.4.1 Local climate from the CAN02 record based on two independent proxies

The temperatures inferred from pollen data with the BRT method based on the TEMPSCAND modern database and brGDGT data with the Bayesian, Mrs and Index1 calibrations show very similar trends through the Holocene (Fig. 9). First, cold conditions are evidenced from 15,000 to 11,700 cal. yrs BP followed from 10,500 to 6,600 cal. BP by warmer conditions (plateau) with temperatures lower than those observed today. Contrary to the BRT and brGDGT signal, the MAT method
485 based on the TEMPSCAND modern database shows a slight thermic optimum from 10,500 to 8,000. After the thermic optimum, a cooling trend until 6,600 cal. BP is evidenced (Fig. 9a). Due to a possible bias during the shaded area, the 6,600 – 5,000 cal. BP period will not be discussed. From 5,000 to 200 cal. BP, a slight warming trend is reconstructed for both proxies. Finally, from 200 cal. BP onward, an abrupt cooling characterizes the brGDGT signal (Fig. 9b), while the pollen signal shows only a slight cooling trend (Fig. 9a).
490 Mid-Holocene temperatures cooler than the present-day ones and followed by a warming (i.e., the inverse of the HTM followed by a cooling), inferred by two independent proxies, appear as a robust reconstruction of mean annual temperatures for Canroute. This climate pattern is consistent with both atmospheric climate model outputs (Mauri et al., 2014; Liu et al., 2014; Wanner et al., 2021; Erb et al., 2022) and pollen-based palaeoclimatic studies (Herzschuh et al., 2022), which depicted a Holocene cooler than today for the same latitudes. According to several studies, the presence of the HTM can result from a

495   seasonality bias toward summer temperatures (Liu et al., 2014; Samartin et al., 2017; Wanner et al., 2021; Herzschuh et al.,

2022).
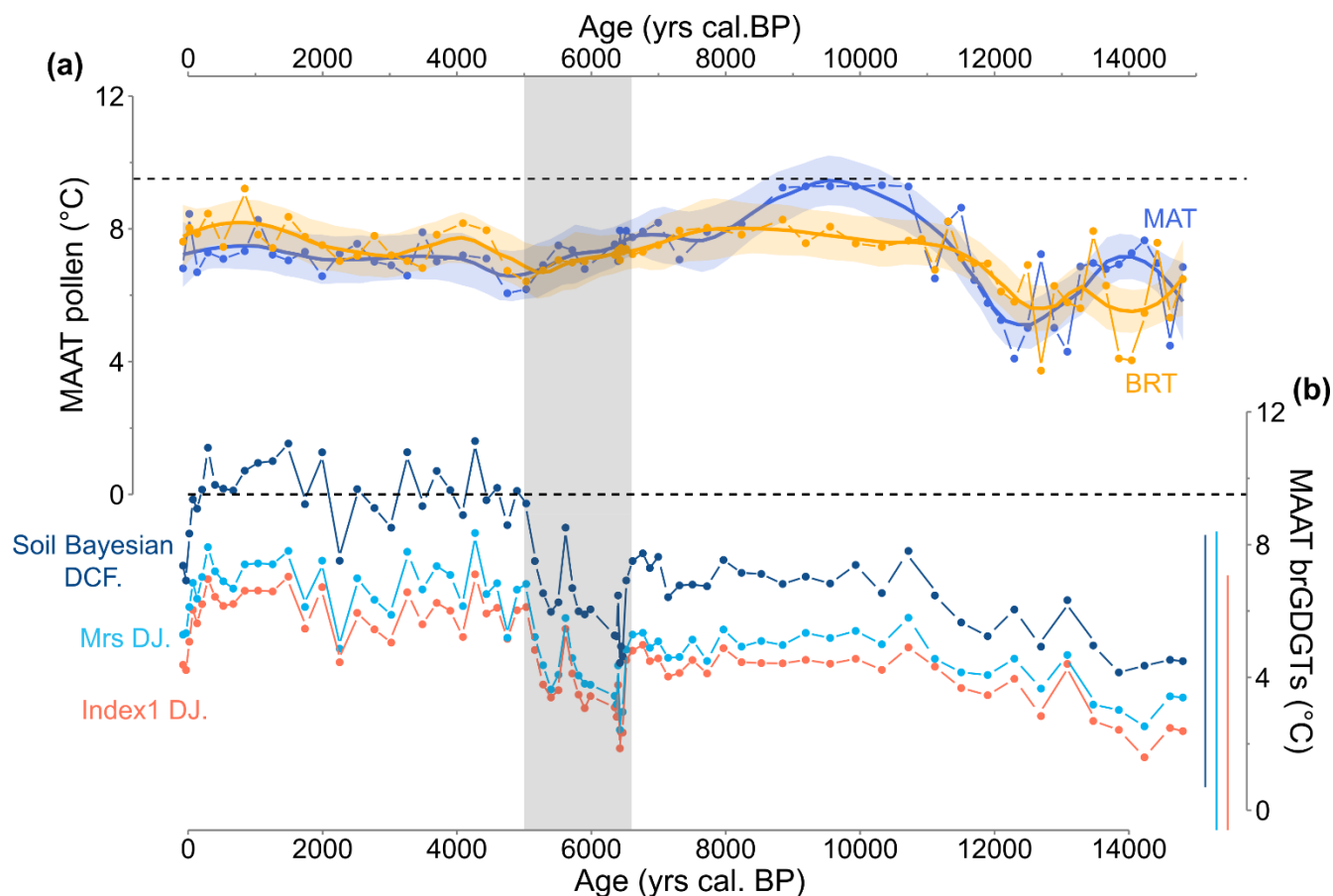
Figure 9: CAN02 temperature reconstructions (MAAT, in °C) from (a) pollen assemblages obtained with BRT (yellow curve) and MAT (blue curve) methods based on the TEMPSCAND calibration. For both curves, the solid line corresponds to locally estimated scatterplot smoothing (loess) regression curves, the shaded area corresponds to its 95 % confidence interval, and (b) brGDGT signal
500   **for the 3 selected soil calibrations: Soil Bayesian DCF. (dark blue), Mrs DJ. (light blue) and Index1 DJ. (red). Calibration errors (RMSE) are represented by lateral lines on the right side. Finally, the black dashed line corresponds to the modern MAAT at Canroute. The shaded period highlights the period of significant decrease in tetramethylated brGDGT abundance (6,600–5,000 cal. BP) and a shift in accumulation rate.**

4.4.2 Regional climate of the northern Mediterranean basin during the last 15,000 years

505   The Canroute climate reconstruction indicates cold conditions for the Lateglacial and a warming for the Early Holocene (about

$+5 \pm 1°$ C, Fig. 10a). A similar climatic trend for this period is reconstructed from chironomid data in northern Italy (Fig. 10a),

with increasing summer temperatures between 14,000 and 10,000 cal. BP of the same order of magnitude (ca. $+6.5°$ C,

Samartin et al., 2017). The brGDGT signal from Canroute indicates an abrupt warming around 13,500 cal. BP, which is

observed slightly earlier (13,700 cal. BP) in southern Italy from the Lake Matese brGDGT record (Fig. 10a, Robles et al.,

510 2022a). The Lateglacial climatic changes estimated from the CAN02 sequence are consistent with observations from southern Europe, notably with the temperature signal of the Lapsou sequence proposed by Duprat-Oualid et al. (2022), located in Cantal (central part of Massif Central). The comparison between the pollen signals from Canroute and Lapsou reveals some similarities (e.g., the chronology of the Bølling-Allerød between 14,600 and 12,900 cal. BP) and some discrepancies (e.g., the dynamics of Younger Dryas is clearly less marked at Canroute). However, the presence of typical Lateglacial events cannot

515 be observed on both proxies as the brGDGT signal does not show such abrupt events (Fig. 10a). Overall, the Lateglacial climate signal trend of Canroute fits well with the more regional signal when confronted with different sites and proxies of southern Europe.

A spatio-temporal heterogeneity of the Holocene climate at the northern Mediterranean region scale is observed when

520 confronting several reconstructions based on different sequences and proxies (Fig. 10). Most of the records indicate, despite a temporal disparity, the presence of a Holocene thermal maximum (HTM) between 10,000 and 6,000 cal. BP. Summer and annual temperatures, reconstructed from the Swiss Alps, Gulf of Lions, Europe (40–50°N), northern Italy and Massif Central (Heiri et al., 2003; Jalali et al., 2016; Samartin et al., 2017; Martin et al., 2020; Herzschuh et al., 2022, Fig. 10b), show a HTM between 10,700 and 5,500 cal. BP. The pollen-based annual temperature of Europe (40–50° N) indicates warm conditions but

525 not really an HTM (Herzschuh et al., 2022, Fig. 10b). When compared to those sequences, only the pollen-based MAT method reconstructs a HTM between 10,000 and 8,000 cal. BP at Canroute, although less marked in terms of anomalies, corresponding with the orbital-induced summer insolation maximum in the northern hemisphere (Laskar et al. 2004; Fig. 10b), but biased by the high percentages of *Corylus* without modern analogues (Fig. 6).

The BRT method and brGDGT-based reconstructions both indicates a plateau with negative anomalies, closer to the annual

530 climate signal proposed by Herzschuh et al. (2022) for Europe (40–50°N) with the WA-PLS (Fig. 10b). From the Mid-Holocene (ca. 6,000 cal. BP) onward, the reconstructions from Canroute and Europe (Davis et al., 2003; Herzschuh et al., 2022) indicate a warming trend, while the data from Massif Central (Martin et al., 2020), Swiss Alps (Heiri et al., 2003), northern Italy (Samartin et al., 2017), and Mediterranean (Jalali et al., 2016, Fig. 10b) indicate a cooling trend following the HTM. The presence of different patterns in the different reconstructions can be explained by the type of parameter

535 reconstructed (SST; MTWA, MAAT etc.), by the method used (local, regional or area-average reconstructions) (Erb et al., 2022), by the proxy itself, but also by local conditions, which can largely influence the proxy record over time. For example, the two reconstructions based on brGDGTs (Fig. 10b) do not indicate the same climate signal. Such difference for the same proxy in the same region (Massif Central) may be due to several factors used to reconstruct the signal: local environment (peatland vs. lake), altitude (790 vs. 1234 m) and calibration (soil vs. lake). On the other side, the studies of Herzschuh et al.

540 (2022), Heiri et al. (2003), Samartin et al. (2017) and Jalali et al. (2016) supports the cooling trend following the HTM and reconstruct seasonal temperatures (summer or July). In the case of the SSTs of the Gulf of Lion proposed by Jalali et al. (2016), the signal is based on alkenones record which could also be biased towards seasonal temperatures (Bader et al., 2020). Additionally, when Canroute's BRT-based signal is compared to the two signals from Herzschuh et al. (2022), i.e., the annual

and July signal, only the annual signal appears consistent with Canroute's signal, the seasonal signal indicating a different trend

545   from 8,000 cal. BP onward (Fig. 10b). This supports the hypothesis of the influence of the seasonal (summer) temperatures in

the cooling trend following the HTM in many studies (Wanner et al., 2021). To conclude, in this study, the influence of

seasonal temperature in different reconstructions, with independent proxies, is a solid hypothesis to explain the presence of

different climatic patterns during the Holocene, particularly for the presence of the Holocene thermic maximum (HTM) in the

Mediterranean region.

550
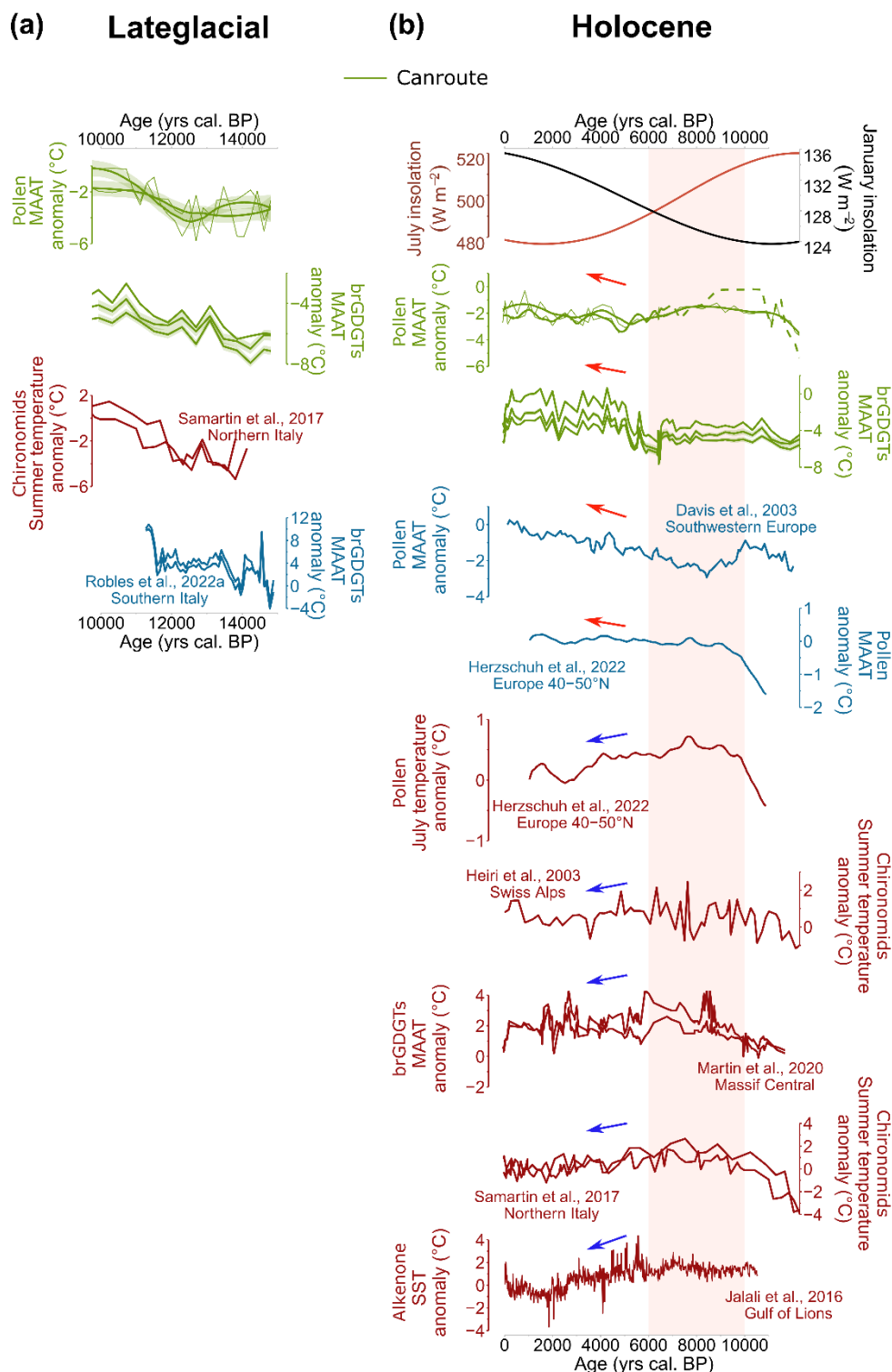
Figure 10: Selected palaeoenvironmental records from southern Europe. (a): Lateglacial climate changes: pollen- and brGDGTs-

based MAATs (Fig. 9); Chironomids-based warmest month temperatures from northern Italy (Samartin et al. 2017); brGDGT-based MAATs from Lake Matese (southern Italy) (Robles et al., 2022a). (b): Holocene climate changes: July and January insolation for 44°N (in W m⁻²) (Laskar et al., 2004); MAATs inferred from CAN02 pollen assemblages (the dashed part corresponds to the period where *Corylus* strongly impacts the results obtained with the MAT and over warmed the HTM) and from brGDGTs; MAAT and summer temperature of the European region (40-50°N) from pollen data (Herzschuh et al., 2022); MAATs based on brGDGTs (Martin et al., 2020); Chironomid-based July temperature (Heiri et al., 2003; Samartin et al. 2017); Pollen-based MAAT for south-western Europe (Davis et a., 2003); Sea Surface Temperature (SST) values of the Gulf of Lions (Jalali et al., 2016). The green (Canroute) and blue curves correspond to annual reconstructed temperatures. The red curves correspond to seasonal (summer) reconstructed temperatures. The red box marks the Holocene thermal maximum of the Northern Hemisphere (HTM). Temperature values are expressed as anomalies from the modern climate conditions at each site.

5 Conclusion

The palaeoclimatic reconstruction of the last 15,000 years based on the CAN02 sequence from a multi-proxy and multi-method approach has allowed us to compare the southern Massif Central climate to the southern Europe one. The Lateglacial and Early Holocene temperature patterns at Canroute are consistent with reconstructions in Italy that show cold conditions during the Lateglacial and a warming for the Early Holocene. During the Holocene, the temperature reconstructed from pollen assemblages with the MAT method is consistent with studies indicating the presence of a Holocene thermal maximum (HTM) between 10,000 and 6,000 cal. BP, although not associated with positive temperature anomalies and biased by the high percentages of *Corylus* without modern analogues. As for the brGDGT signal and the BRT-based method, it shows the presence of a Mid-Holocene plateau followed by a late-Holocene warming instead of a clear mid-Holocene thermal maximum (HTM). The similar trends between the two independent proxies supports the reliability of their respective reconstructions. Our study also highlights the potential causes of the differences between the reconstructions from independent proxies. The influence of local context changes, such as a decrease in water input, on the vegetation and brGDGT records, has been assessed from geochemical, pollen and brGDGT records. The multi-proxy approach points out the importance of investigating changes in the local environmental context for a better interpretation of the reconstructed climate parameters, as those changes could impact pollen and brGDGT records and thus the quality of the reconstructed climate parameters.

Whether for pollen or brGDGTs, the calibration of modern data to reconstruct climate parameters is a key step and has a significant role in the reliability of reconstructions. Studies have shown that regional calibration increases the reliability of reconstructed MAATs. A selection of European surface samples from the global peat and soil calibrations could improve the reliability of MAAT reconstructions.

Appendices

Appendix A

Table A: Location and mean current climate values of sites associated with surface samples for brGDGT analysis. The current climate parameters were extracted with the GIS software QGIS (QGIS.org 2022) from the interpolated database WorldClim2.0 (averaged over the period 1970–2000, Fick and Hijmans, 2017) for annual temperature (MAAT) and precipitation (MAP) data and the CRU TS (version 4.06) measured database (Harris et al., 2020) for monthly temperature and precipitation data (Fig. 1c).

Peatland	Localization	Sample	Elevation (m)	MAAT (°C)	MAP (mm)
Canroute	43°38'48" N 02°34'35" E	CAN0	790	9.5	895
Caroux	43°35'59" N 02°58'25" E	CAR-1-15	1090	9.1	1044
Caroux	43°36'06" N 02°59'01' E	CAR-C2	1090	9.8	1078
Lapsou	45°04'39" N 03°44'44" E	LAP	1200	8.7	697
Lozère	44°27'01" N 03°38'01' E	LOZ	1700	5.5	1534
Nassette	44°28'11" N 03°37'27" E	NAS	1320	5.9	1445
Nassette	44°28'11" N 03°37'27" E	NAS-21	1320	5.9	1445

Appendix B
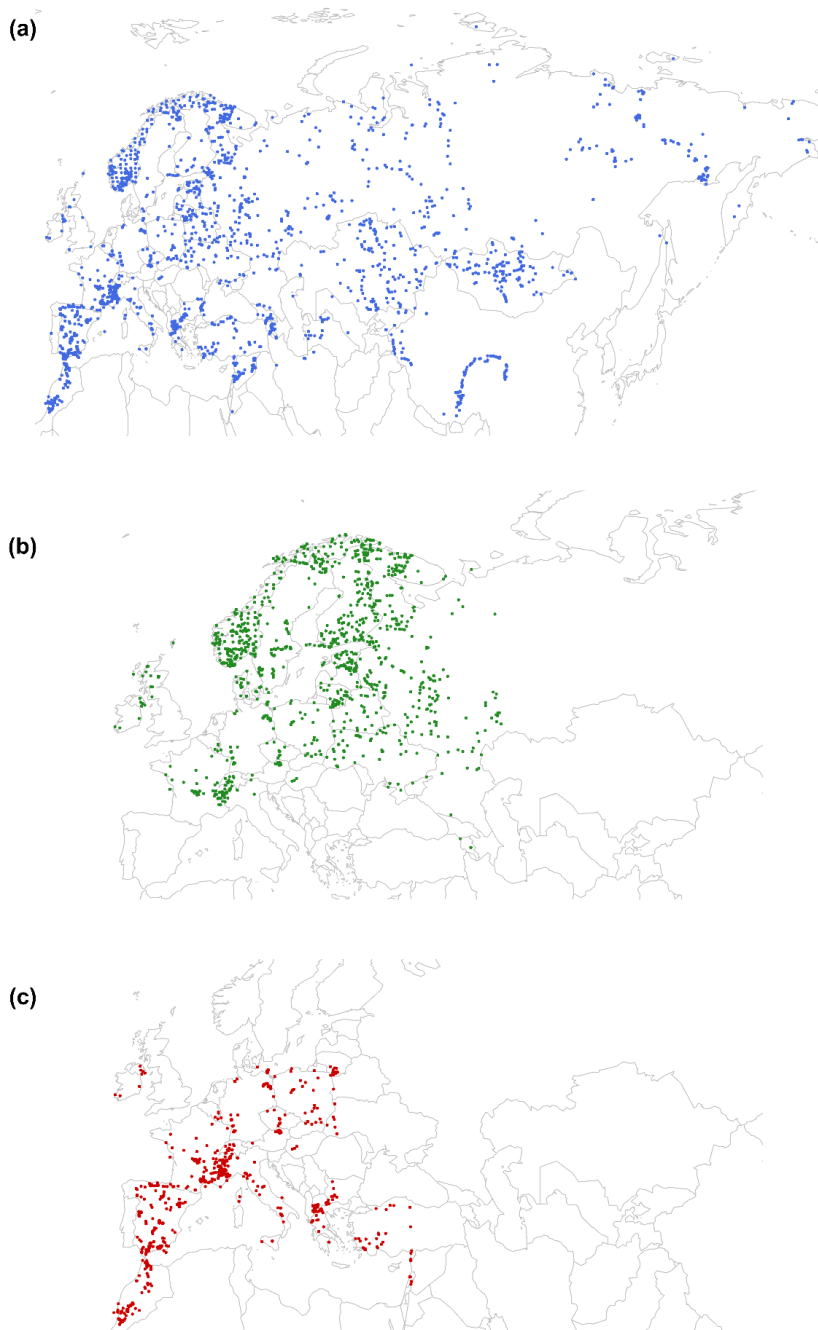
590 **Figure B:** **Location of surface sites used in (a) the Eurasian Pollen Database (EAPDB) compiled by Peyron et al. (2013, 2017); (b) the TEMPSCAND (Temperate Europe and Scandinavia) database; (c) the MEDTEMP (Mediterranean and Temperate Europe) database.**

595   **Appendix C**
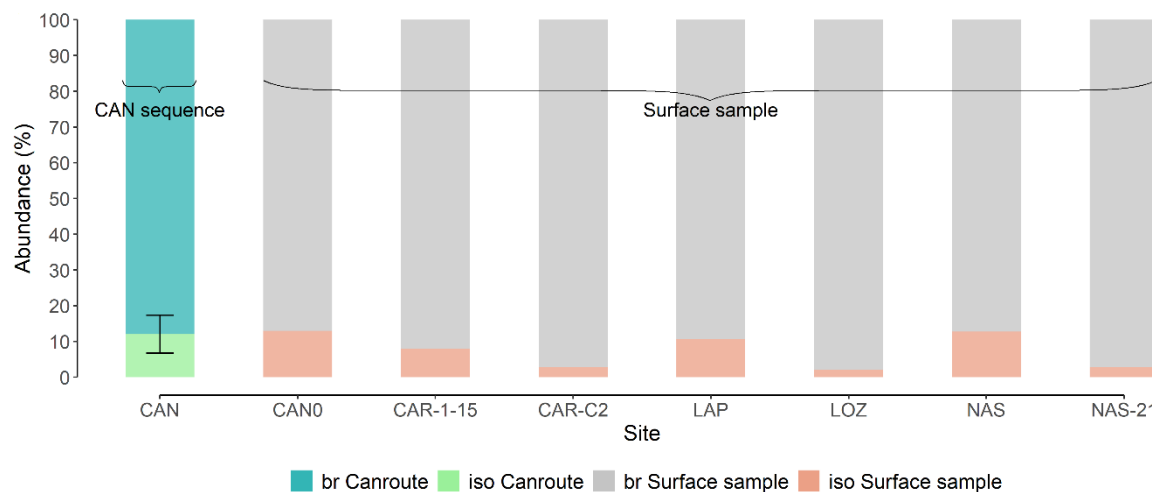
Figure C: Relative abundance (%) of isoGDGTs (pink) and brGDGTs (grey) for surface samples and average relative abundance of isoGDGTs (green) and brGDGTs (blue) in the CAN core (*n* = 75).

Appendix D
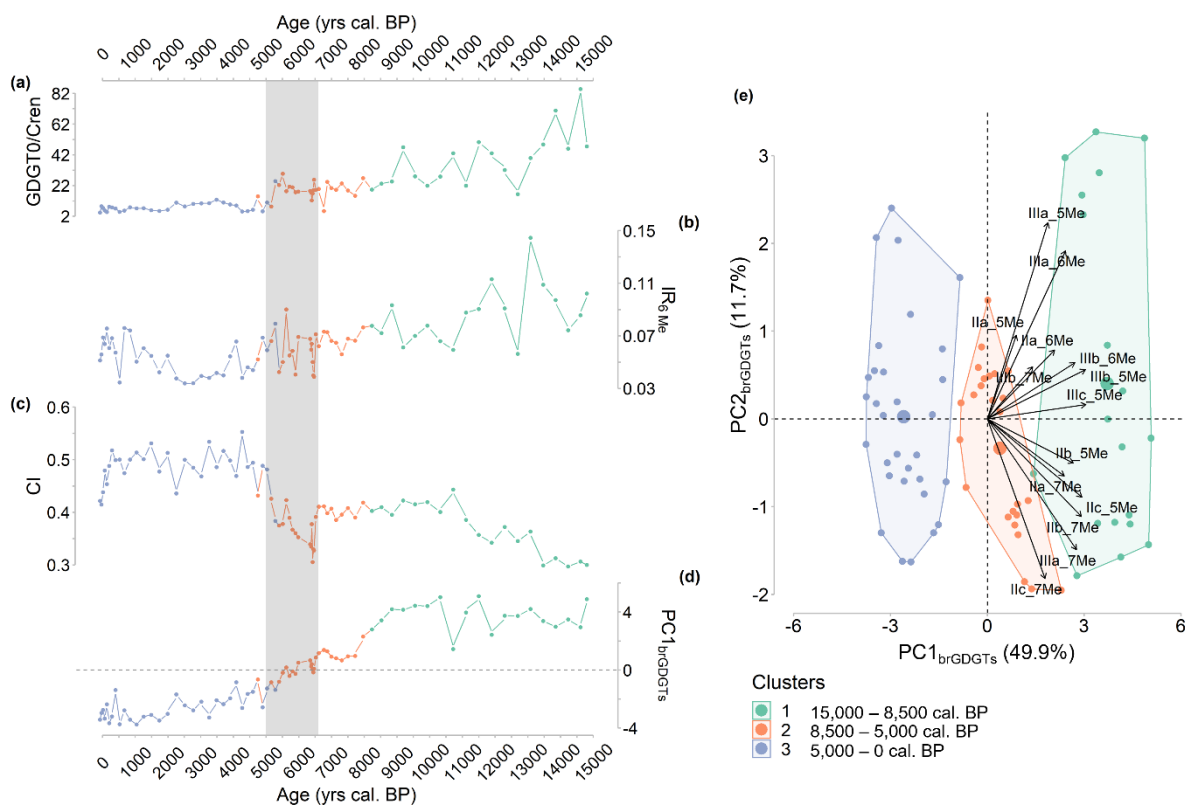
600 **Figure D: (a): GDGT-0/Cren ratio. (b): Isomer Ratio (IR$_{6Me}$). (c): Bacterial Community Index (CI) through time. (d): PC1$_{brGDGTs}$ of the PCA performed on the brGDGT relative abundances of the Canroute sequence, (e): PCA results with samples coloured according to the cluster to which they belong.**

Appendix E
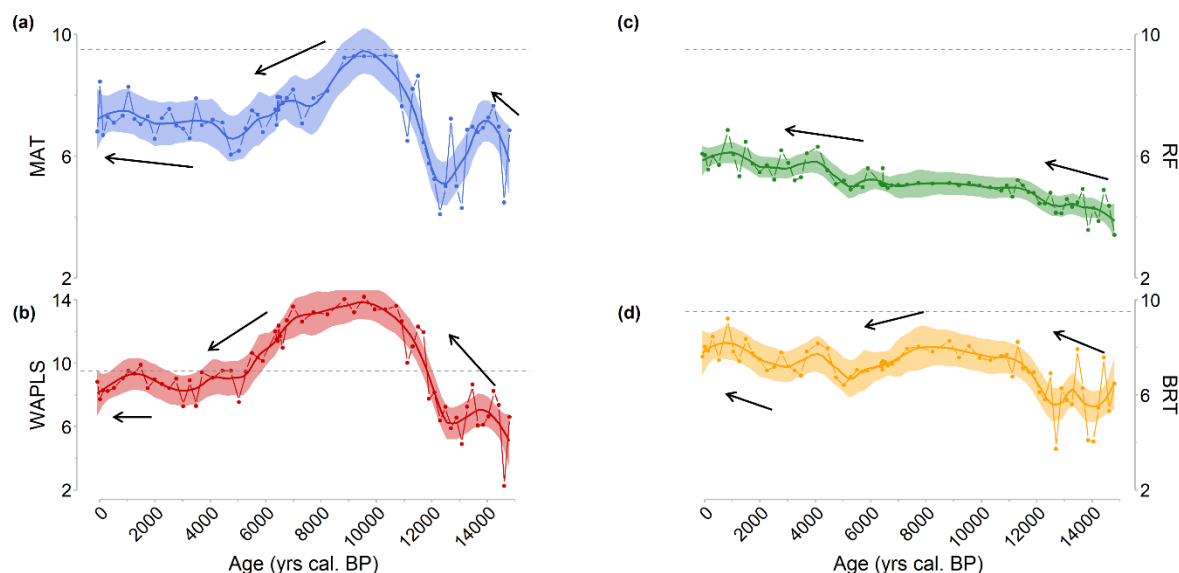
Figure E: Reconstruction of the mean annual air temperature (MAAT) based on Canroute pollen sequence signal for the four
605 **methods used with the EAPDB modern pollen database ((a): MAT, (b): WA-PLS, (c): RF, (d): BRT). The plain line corresponds to locally estimated scatterplot smoothing (loess) regression curves, the shaded area corresponds to the confidence interval used for the model (95 %). The black arrows represent the direction of the climate trends for the different periods considered. Black dashed line: current MAAT at Canroute.**

Data availability

610 BrGDGTs analysis and pollen-inferred climate reconstruction will be fully available; the pollen counts will be shared thanks to open international databases as EPD, or Neotoma.

Author contribution

Ld performed the analytical work with LD and JA designing R codes. Ld, LD, GM, AE, OP designed the study. LD, GM, AE and OP supervised the study. SDM and LB provided the study material (CAN02 sequence). SDM, CB, LB, SAA and MS
615 contributed to data analysis. AE provided financial support for the project. All authors contributed to the writing of the manuscript.

Competing interests

The authors declare that they have no conflict of interest.

Acknowledgements

620 This study is a part of the DEMETER project supported by the European Research Council (ERC) under the European Union's Horizon 2020 research and innovation programme (grant agreement No. 852573, PI A. Evin). The sampling of peat cores and surface samples was performed during field schools of the University of Montpellier, as part of ORPAM teaching modules. The authors thank Frédéric Néri and the CEN Languedoc-Roussillon for fieldwork facilities, ISEM for financial contribution to radiocarbon dating, Sandrine Canal for the preparation and treatment of pollen samples, and Jean-Frédéric Terral, Vincent

625 Girard and ORPAM students for help with fieldwork and with the preliminary study of the Canroute Peatland. This is ISEM contribution XXX-XXXX.

References

Ardenghi, N., Mulch, A., Koutsodendris, A., Pross, J., Kahmen, A., and Niedermeyer, E. M.: Temperature and moisture variability in the eastern Mediterranean region during Marine Isotope Stages 11–10 based on biomarker analysis of the Tenaghi

630 Philippon peat deposit, Quaternary Science Reviews, 225, 105977, https://doi.org/10.1016/j.quascirev.2019.105977, 2019.

Ball, D. F.: Loss-on-ignition as an estimate of organic matter and organic carbon in non-calcareous soils, Journal of Soil Science, 15, 84–92, https://doi.org/10.1111/j.1365-2389.1964.tb00247.x, 1964.

de Beaulieu, J.-L.: Contribution pollenanalytique à l'histoire tardiglaciaire et holocène des Alpes méridionales françaises. Doctoral Thesis, Université d'Aix-Marseille III, France, 358 p., 1977.

635 de Beaulieu, J.-L., and Reille, M.: Paléoenvironnement tardiglaciaire et holocène des lacs de Pelléautier et Siguret (Hautes-Alpes, France). I. Histoire de la végétation d'après les analyses polliniques, Ecologia Mediterranea 9 (3-4), 19–36, 1983.

Birks, H. J. B. and Seppä, H.: Pollen-based reconstructions of late-Quaternary climate in Europe – progress, problems, and pitfalls, Acta Palaeobotanica, 44, 317–334, 2004.

Birks, H. H. and Birks, H. J. B.: Multi-proxy studies in palaeolimnology, Veget Hist Archaeobot, 15, 235–251,

640 https://doi.org/10.1007/s00334-006-0066-6, 2006.

Blaauw, M., Christen, J. A., Vázquez, J. E., & Goring, S.: clam: Classical age-depth modelling of cores from deposits, R package version 2.5.0, 2(4), 2022.

Blaga, C. I., Reichart, G.-J., Heiri, O., and Sinninghe Damsté, J. S.: Tetraether membrane lipid distributions in water-column particulate matter and sediments: a study of 47 European lakes along a north–south transect, J Paleolimnol, 41, 523–540,

645 https://doi.org/10.1007/s10933-008-9242-2, 2009.

Breiman, L.: Random Forests, Machine Learning, 45, 5–32, https://doi.org/10.1023/A:1010933404324, 2001.

Broecker, W. S., Denton, G. H., Edwards, R. L., Cheng, H., Alley, R. B., and Putnam, A. E.: Putting the Younger Dryas cold event into context, Quaternary Science Reviews 29, 1078–1081, 2010.

Cartapanis, O., Jonkers, L., Moffa-Sanchez, P., Jaccard, S. L., and de Vernal, A.: Complex spatio-temporal structure of the
650   Holocene thermal maximum, Nat Commun, 13, 5662, https://doi.org/10.1038/s41467-022-33362-1, 2022.

Cheddadi, R., Yu, G., Guiot, J., Harrison, S. P., and Prentice, I. C.: The climate of Europe 6000 years ago, Climate Dynamics, 13, 1–9, https://doi.org/10.1007/s003820050148, 1997.

Chevalier, M., Davis, B. A. S., Heiri, O., Seppä, H., Chase, B. M., Gajewski, K., Lacourse, T., Telford, R. J., Finsinger, W., Guiot, J., Kühl, N., Maezumi, S. Y., Tipton, J. R., Carter, V. A., Brussel, T., Phelps, L. N., Dawson, A., Zanon, M., Vallé, F.,
655   Nolan, C., Mauri, A., de Vernal, A., Izumi, K., Holmström, L., Marsicek, J., Goring, S., Sommer, P. S., Chaput, M., and Kupriyanov, D.: Pollen-based climate reconstruction techniques for late Quaternary studies, Earth-Science Reviews, 210, 33, 2020.

Davis, B. A. S., Brewer, S., Stevenson, A. C., and Guiot, J.: The temperature of Europe during the Holocene reconstructed from pollen data, Quaternary Science Reviews, 22, 1701–1716, https://doi.org/10.1016/S0277-3791(03)00173-2, 2003.

660   Davtian, N., Bard, E., Darfeuil, S., Ménot, G., and Rostek, F.: The Novel Hydroxylated Tetraether Index RI-OH′ as a Sea Surface Temperature Proxy for the 160-45 ka BP Period Off the Iberian Margin, Palaeoceanography and Palaeoclimatology, 36, e2020PA004077, https://doi.org/10.1029/2020PA004077, 2021.

De Jonge, C., Kuramae, E. E., Radujković, D., Weedon, J. T., Janssens, I. A., and Peterse, F.: The influence of soil chemistry on branched tetraether lipids in mid- and high latitude soils: Implications for brGDGT- based palaeothermometry, Geochimica
665   et Cosmochimica Acta, 310, 95–112, https://doi.org/10.1016/j.gca.2021.06.037, 2021.

De Jonge, C., Stadnitskaia, A., Hopmans, E. C., Cherkashov, G., Fedotov, A., and Sinninghe Damsté, J. S.: In situ produced branched glycerol dialkyl glycerol tetraethers in suspended particulate matter from the Yenisei River, Eastern Siberia, Geochimica et Cosmochimica Acta, 125, 476–491, https://doi.org/10.1016/j.gca.2013.10.031, 2014a.

De Jonge, C., Hopmans, E. C., Zell, C. I., Kim, J.-H., Schouten, S., and Sinninghe Damsté, J. S.: Occurrence and abundance
670   of 6-methyl branched glycerol dialkyl glycerol tetraethers in soils: Implications for palaeoclimate reconstruction, Geochimica et Cosmochimica Acta, 141, 97–112, https://doi.org/10.1016/j.gca.2014.06.013, 2014b.

De Jonge, C., Radujkovic´, D., Sigurdsson, B. D., Weedon, J. T., Janssens, I., and Peterse, F.: Lipid biomarker temperature proxy responds to abrupt shift in the bacterial community composition in geothermally heated soils, Organic Geochemistry, 137, 103897, https://doi.org/10.1016/j.orggeochem.2019.07.0006,2019.

675   Dearing Crampton-Flood, E., Tierney, J. E., Peterse, F., Kirkels, F. M. S. A., and Sinninghe Damsté, J. S.: BayMBT: A Bayesian calibration model for branched glycerol dialkyl glycerol tetraethers in soils and peats, Geochimica et Cosmochimica Acta, 268, 142–159, https://doi.org/10.1016/j.gca.2019.09.043, 2020.

De'ath, G.: Boosted Trees for Ecological. Modelling and Prediction, Ecology, 88, 243–251, https://doi.org/10.1890/0012-9658(2007)88[243:BTFEMA]2.0.CO;2, 2007.

680   Decorsiere, J., Delamare-Deboutteville, J. and Lecerf, C.: Reconstitution de 13 500 ans d'histoire d'une tourbière dans le Sud de la France. Orpalm Synthesis, 12, 29–39, 2019.

Denton, G. H., Anderson, R. F., Toggweiler, J. R., Edwards, R. L., Schaefer, J. M., and Putnam, A. E.: The Last Glacial Termination, Science 328, 1652–1656, 2010.

Dugerdil, L., Joannin, S., Peyron, O., Jouffroy-Bapicot, I., Vannière, B., Boldgiv, B., Unkelbach, J., Behling, H., and Ménot,

685   G.: Climate reconstructions based on GDGT and pollen surface databases from Mongolia and Baikal area: calibrations and applicability to extremely cold–dry environments over the Late Holocene, Clim. Past, 17, 1199–1226, https://doi.org/10.5194/cp-17-1199-2021,2021a.

Dugerdil, L., Ménot, G., Peyron, O., Jouffroy-Bapicot, I., Ansanay-Alex, S., Antheaume, I., Behling, H., Boldgiv, B., Develle, A.-L., Grossi, V., Magail, J., Makou, M., Robles, M., Unkelbach, J., Vannière, B., and Joannin, S.: Late Holocene Mongolian

690   climate and environment reconstructions from brGDTs, NPPs and pollen transfer functions for Lake Ayrag: Palaeoclimate implications for Arid Central Asia, Quaternary Science Reviews, 273, 107235, https://doi.org/10.1016/j.quascirev.2021.107235, 2021b.

Duprat-Oualid, F., Bégeot, C., Peyron, O., Rius, D., Millet, L., and Magny, M.: High-frequency vegetation and climatic changes during the Lateglacial inferred from the Lapsou pollen record (Cantal, southern Massif Central, France), Quaternary

695   International, 636, 69–80, https://doi.org/10.1016/j.quaint.2022.04.012, 2022.

Elith, J., Leathwick, J. R., and Hastie, T.: A working guide to boosted regression trees, Journal of Animal Ecology, 77, 802–813, https://doi.org/10.1111/j.1365-2656.2008.01390.x, 2008.

Erb, M. P., McKay, N. P., Steiger, N., Dee, S., Hancock, C., Ivanovic, R. F., Gregoire, L. J., and Valdes, P.: Reconstructing Holocene temperatures in time and space using palaeoclimate data assimilation, Clim. Past, 18, 2599–2629,

700   https://doi.org/10.5194/cp-18-2599-2022, 2022.

Fick, S. E. and Hijmans, R. J.: WorldClim 2: new 1-km spatial resolution climate surfaces for global land areas, International Journal of Climatology, 37, 4302–4315, https://doi.org/10.1002/joc.5086, 2017.

Grimm, E. C.: CONISS: a FORTRAN 77 program for stratigraphically constrained cluster analysis by the method of incremental sum of squares, Computers & Geosciences, 13, 13–35, https://doi.org/10.1016/0098-3004(87)90022-7, 1987.

705   Guiot, J.: Methodology of the last climatic cycle reconstruction in France from pollen data, Palaeogeography, Palaeoclimatology, Palaeoecology, 80, 49–69, https://doi.org/10.1016/0031-0182(90)90033-4, 1990.

Harris, I., Osborn, T. J., Jones, P., and Lister, D.: Version 4 of the CRU TS monthly high-resolution gridded multivariate climate database, Sci Data, 7, 109, https://doi.org/10.1038/s41597-020-0453-3, 2020.

Heiri, O., Lotter, A. F., Hausmann, S., and Kienast, F.: A chironomid-based Holocene summer air temperature reconstruction

710   from the Swiss Alps, The Holocene, 13, 477–484, https://doi.org/10.1191/0959683603hl640ft, 2003.

Herzschuh, U., Böhmer, T., Chevalier, M., Dallmeyer, A., Li, C., Cao, X., Hébert, R., Peyron, O., Nazarova, L., Novenko, E. Y., Park, J., Rudaya, N. A., Schlütz, F., Shumilovskikh, L. S., Tarasov, P. E., Wang, Y., Wen, R., Xu, Q., and Zheng, Z.:

Regional pollen-based Holocene temperature and precipitation patterns depart from the Northern Hemisphere mean trends, Atmospheric Dynamics/Terrestrial Archives/Holocene, https://doi.org/10.5194/egusphere-2022-127, 2022.

715 Hijmans, R. J., Phillips, S., Leathwick, J., Elith, J.: Package "dismo", Circles, 9, 1-68, 2017.

Hopmans, E. C., Weijers, J. W. H., Schefuß, E., Herfort, L., Sinninghe Damsté, J. S., and Schouten, S.: A novel proxy for terrestrial organic matter in sediments based on branched and isoprenoid tetraether lipids, Earth and Planetary Science Letters, 224, 107–116, https://doi.org/10.1016/j.epsl.2004.05.012, 2004.

Hopmans, E. C., Schouten, S., and Sinninghe Damsté, J. S.: The effect of improved chromatography on GDGT-based 720 palaeoproxies, Organic Geochemistry, 93, 1–6, https://doi.org/10.1016/j.orggeochem.2015.12.006, 2016.

Huguet, A., Fosse, C., Laggoun-Défarge, F., Toussaint, M.-L., and Derenne, S.: Occurrence and distribution of glycerol dialkyl glycerol tetraethers in a French peat bog, Organic Geochemistry, 41, 559–572, https://doi.org/10.1016/j.orggeochem.2010.02.015, 2010.

Huguet, C., Hopmans, E. C., Febo-Ayala, W., Thompson, D. H., Sinninghe Damsté, J. S., and Schouten, S.: An improved 725 method to determine the absolute abundance of glycerol dibiphytanyl glycerol tetraether lipids, Organic Geochemistry, 37, 1036–1041, https://doi.org/10.1016/j.orggeochem.2006.05.008, 2006.

Jalali, B., Sicre, M.-A., Bassetti, M.-A., and Kallel, N.: Holocene climate variability in the North-Western Mediterranean Sea (Gulf of Lions), Clim. Past, 12, 91–101, https://doi.org/10.5194/cp-12-91-2016, 2016.

Joosten, H.: Current soil carbon loss and land degradation globally: where are the hotspots and why there?, Soil carbon: science, 730 management and policy for multiple benefits, 224–234, https://doi.org/10.1079/9781780645322.0224, 2015.

Josse, J. and Husson, F.: missMDA: A Package for Handling Missing Values in Multivariate Data Analysis, Journal of Statistical Software, 70, 1-31, https://doi:10.18637/jss.v070.i01, 2016.

Juggins, S. and Juggins, M. S.: Package 'rioja'. An R Package for the Analysis of Quaternary Science Data., 0.9, 26, 2020.

Kassambara, A., and Mundt, F.: Factoextra: extract and visualize the results of multivariate data analyses, R package version, 735 1, 337-354, 2017.

Kaufman, D., McKay, N., Routson, C., Erb, M., Dätwyler, C., Sommer, P. S., Heiri, O., and Davis, B.: Holocene global mean surface temperature, a multi-method reconstruction approach, Sci Data, 7, 201, https://doi.org/10.1038/s41597-020-0530-7, 2020.

Laskar, J., Robutel, P., Joutel, F., Gastineau, M., Correia, A. C. M., and Levrard, B.: A long-term numerical solution for the 740 insolation quantities of the Earth, A&A, 428, 261–285, https://doi.org/10.1051/0004-6361:20041335, 2004.

Le, S., Josse, J., and Husson, F.: FactoMineR: An R Package for Multivariate Analysis, Journal of Statistical Software, 25(1), 1–18, https://www.jstatsoft.org/v25/i01/, 2008.

Le Houérou, H.-N.: Biogeography of the arid steppeland north of the Sahara, Journal of Arid Environments, 48, 103–128, 2001.

745 Li, J., Pancost, R. D., Naafs, B. D. A., Yang, H., Zhao, C., and Xie, S.: Distribution of glycerol dialkyl glycerol tetraether (GDGT) lipids in a hypersaline lake system, Organic Geochemistry, 99, 113–124, https://doi.org/10.1016/j.orggeochem.2016.06.007, 2016.

Liu, Z., Zhu, J., Rosenthal, Y., Zhang, X., Otto-Bliesner, B. L., Timmermann, A., Smith, R. S., Lohmann, G., Zheng, W., and Elison Timm, O.: The Holocene temperature conundrum, Proc. Natl. Acad. Sci. U.S.A., 111,
750 https://doi.org/10.1073/pnas.1407229111, 2014.

Marcott, S. A., Shakun, J. D., Clark, P. U., and Mix, A. C.: A Reconstruction of Regional and Global Temperature for the Past 11,300 Years, Science, 339, 1198–1201, https://doi.org/10.1126/science.1228026, 2013.

Marriner, N., Kaniewski, D., Pourkerman, M., and Devillers, B.: Anthropocene tipping point reverses long-term Holocene cooling of the Mediterranean Sea: A meta-analysis of the basin's Sea Surface Temperature records, Earth-Science Reviews,
755 227, 103986, https://doi.org/10.1016/j.earscirev.2022.103986, 2022.

Marsicek, J., Shuman, B. N., Bartlein, P. J., Shafer, S. L., and Brewer, S.: Reconciling divergent trends and millennial variations in Holocene temperatures, Nature, 554, 19, https://doi.org/doi:10.1038/nature25464, 2018.

Martin, C., Ménot, G., Thouveny, N., Davtian, N., Andrieu-Ponel, V., Reille, M., and Bard, E.: Impact of human activities and vegetation changes on the tetraether sources in Lake St Front (Massif Central, France), Organic Geochemistry, 135, 38–52,
760 https://doi.org/10.1016/j.orggeochem.2019.06.005, 2019.

Martin, C., Ménot, G., Thouveny, N., Peyron, O., Andrieu-Ponel, V., Montade, V., Davtian, N., Reille, M., and Bard, E.: Early Holocene thermal maximum recorded by branched tetraethers and pollen in Western Europe (Massif Central, France), Quaternary Science Reviews, 228, 106109, https://doi.org/10.1016/j.quascirev.2019.106109, 2020.

Mauri, A., Davis, B. A. S., Collins, P. M., and Kaplan, J. O.: The influence of atmospheric circulation on the mid-Holocene
765 climate of Europe: a data–model comparison, Clim. Past, 10, 1925–1938, https://doi.org/10.5194/cp-10-1925-2014, 2014.

Mauri, A., Davis, B. A. S., Collins, P. M., and Kaplan, J. O.: The climate of Europe during the Holocene: a gridded pollen-based reconstruction and its multi-proxy evaluation, Quaternary Science Reviews, 112, 109–127, https://doi.org/10.1016/j.quascirev.2015.01.013, 2015.

Mayewski, P. A., Rohling, E. E., Curt Stager, J., Karlén, W., Maasch, K. A., Meeker, L. D., Meyerson, E. A., Gasse, F., van
770 Kreveld, S., Holmgren, K., Lee-Thorp, J., Rosqvist, G., Rack, F., Staubwasser, M., Schneider, R. R., and Steig, E. J.: Holocene climate variability, Quat. res., 62, 243–255, https://doi.org/10.1016/j.yqres.2004.07.001, 2004.

Miras, Y., Vergne, V., Guenet, P., and Surmely, F.: Le Massif Central : premières traces d'anthropisation révélées par l'analyse pollinique des zones humides corrélées aux données archéologiques. In: Richard, H. (Dir.), Néolithisation précoce. Premières traces d'anthropisation du couvert végétal à partir des données polliniques. Presses Universitaires Franc-Comtoises, Besançon,
775 pp. 89–105, 2004.

Moore, P.D.: The ecology of peat-forming processes: a review, International Journal of Coal Geology, 12(1-4), 89-103, 1989.

Muller, S.D., Brémond, L., Girard, V., Terral, J.-F.: Végétation de la tourbière de Canroute, dans les Monts de Lacaune (Le Margnès, Tarn), Orpalm Synthesis, 11(1), 9-13, 2018.

Naafs, B. D. A., Inglis, G. N., Zheng, Y., Amesbury, M. J., Biester, H., Bindler, R., Blewett, J., Burrows, M. A., del Castillo
780   Torres, D., Chambers, F. M., Cohen, A. D., Evershed, R. P., Feakins, S. J., Gałka, M., Gallego-Sala, A., Gandois, L., Gray, D. M., Hatcher, P. G., Honorio Coronado, E. N., Hughes, P. D. M., Huguet, A., Könönen, M., Laggoun-Défarge, F., Lähteenoja, O., Lamentowicz, M., Marchant, R., McClymont, E., Pontevedra-Pombal, X., Ponton, C., Pourmand, A., Rizzuti, A. M., Rochefort, L., Schellekens, J., De Vleeschouwer, F., and Pancost, R. D.: Introducing global peat-specific temperature and pH calibrations based on brGDGT bacterial lipids, Geochimica et Cosmochimica Acta, 208, 285–301,
785   https://doi.org/10.1016/j.gca.2017.01.038, 2017a.

Naafs, B. D. A., Gallego-Sala, A. V., Inglis, G. N., and Pancost, R. D.: Refining the global branched glycerol dialkyl glycerol tetraether (brGDGT) soil temperature calibration, Organic Geochemistry, 106, 48–56, https://doi.org/10.1016/j.orggeochem.2017.01.009, 2017b.

Naafs, B. D. A., Inglis, G. N., Blewett, J., McClymont, E. L., Lauretano, V., Xie, S., Ever- shed, R. P., and Pancost, R. D.:
790   The potential of biomarker proxies to trace climate, vegetation, and biogeochemical. processes in peat: A review, Global and Planetary Change, 179, 57–79, https://doi.org/10.1016/j.gloplacha.2019.05.006, 2019.

NASA JPL.: NASA Shuttle Radar Topography Mission Global 1 arc second [Data set], NASA EOSDIS Land Processes DAAC, 2013

Pearson, A. and Ingalls, A. E.: Assessing the Use of Archaeal Lipids as Marine Environmental Proxies, Annual Review of
795   Earth and Planetary Sciences, 41, 359–384, https://doi.org/10.1146/annurev-earth-050212-123947, 2013.

Pearson, E. J., Juggins, S., Talbot, H. M., Weckström, J., Rosén, P., Ryves, D. B., Roberts, S. J., and Schmidt, R.: A lacustrine GDGT-temperature calibration from the Scandinavian Arctic to Antarctic: Renewed potential for the application of GDGT-palaeothermometry in lakes, Geochimica et Cosmochimica Acta, 75, 6225–6238, https://doi.org/10.1016/j.gca.2011.07.042, 2011.

800 Peterse, F., van der Meer, J., Schouten, S., Weijers, J. W. H., Fierer, N., Jackson, R. B., Kim, J.- H., and Sinninghe Damsté, J. S.: Revised calibration of the MBT–CBT palaeotemperature proxy based on branched tetraether membrane lipids in surface soils, Geochimica et Cosmochimica Acta, 96, 215–229, https://doi.org/10.1016/j.gca.2012.08.011, 2012.

Peyron, O., Bégeot, C., Brewer, S., Heiri, O., Magny, M., Millet, L., Ruffaldi, P., Van Campo, E., and Yu, G.: Late-Glacial climatic changes in Eastern France (Lake Lautrey) from pollen, lake-levels, and chironomids, Quat. res., 64, 197–211,
805   https://doi.org/10.1016/j.yqres.2005.01.006, 2005.

Peyron, O., Magny, M., Goring, S., Joannin, S., de Beaulieu, J.-L., Brugiapaglia, E., Sadori, L., Garfi, G., Kouli, K., Ioakim, C., and Combourieu-Nebout, N.: Contrasting patterns of climatic changes during the Holocene across the Italian Peninsula reconstructed from pollen data, Clim. Past, 9, 1233–1252, https://doi.org/10.5194/cp-9-1233-2013, 2013.

Peyron, O., Combourieu-Nebout, N., Brayshaw, D., Goring, S., Andrieu-Ponel, V., Desprat, S., Fletcher, W., Gambin, B.,
810   Ioakim, C., Joannin, S., Kotthoff, U., Kouli, K., Montade, V., Pross, J., Sadori, L., and Magny, M.: Precipitation changes in the Mediterranean basin during the Holocene from terrestrial and marine pollen records: a model-data comparison, Clim. Past, 13, 249–265, https://doi.org/10.5194/cp-13-249-2017, 2017.

Peyron, O., Goring, S., Dormoy, I., Kotthoff, U., Pross, J., de Beaulieu, J.-L., Drescher-Schneider, R., Vannière, B., and Magny, M.: Holocene seasonality changes in the central Mediterranean region reconstructed from the pollen sequences of

815   Lake Accesa (Italy) and Tenaghi Philippon (Greece), The Holocene, 21, 131–146, https://doi.org/10.1177/0959683610384162, 2011.

Ponel, P., Guiter, F., Gandouin, E., Peyron, O., and de Beaulieu, J.-L.: Late-Glacial palaeotemperatures and palaeoprecipitations in the Aubrac Mountains (French Massif Central) reconstructed from multiproxy analyses (Coleoptera, chironomids and pollen), Quaternary International, https://doi.org/10.1016/j.quaint.2022.02.005, 2022.

820   Prasad, A. M., Iverson, L. R., and Liaw, A.: Newer Classification and Regression Tree Techniques: Bagging and Random Forests for Ecological. Prediction, Ecosystems, 9, 181–199, https://doi.org/10.1007/s10021-005-0054-1, 2006.

QGIS.org.: QGIS Geographic Information System. QGIS Association, https://www.qgis.org/, 2022.

R Core Team: R: A language and environment for statistical computing, R Foundation for Statistical Computing, Vienna, Austria, https://www.R-project.org, 2022.

825   Raberg, J. H., Miller, G. H., Geirsdóttir, Á., and Sepúlveda, J.: Near-universal trends in brGDGT lipid distributions in nature, Sci. Adv., 8, eabm7625, https://doi.org/10.1126/sciadv.abm7625, 2022.

Ramos-Román, M. J., De Jonge, C., Magyari, E., Veres, D., Ilvonen, L., Develle, A.-L., and Seppä, H.: Lipid biomarker (brGDGT)- and pollen-based reconstruction of temperature change during the Middle to Late Holocene transition in the Carpathians, Global and Planetary Change, 215, 103859, https://doi.org/10.1016/j.gloplacha.2022.103859, 2022.

830   Rao, Z., Guo, H., Wei, S., Cao, J., and Jia, G.: Influence of water conditions on peat brGDGTs: A modern investigation and its palaeoclimatic implications, Chemical Geology, 606, 120993, https://doi.org/10.1016/j.chemgeo.2022.120993, 2022.

Reimer, P. J., Austin, W. E. N., Bard, E., Bayliss, A., Blackwell, P. G., Bronk Ramsey, C., Butzin, M., Cheng, H., Edwards, R. L., Friedrich, M., Grootes, P. M., Guilderson, T. P., Hajdas, I., Heaton, T. J., Hogg, A. G., Hughen, K. A., Kromer, B., Manning, S. W., Muscheler, R., Palmer, J. G., Pearson, C., van der Plicht, J., Reimer, R. W., Richards, D. A., Scott, E. M.,

835   Southon, J. R., Turney, C. S. M., Wacker, L., Adolphi, F., Büntgen, U., Capano, M., Fahrni, S. M., Fogtmann-Schulz, A., Friedrich, R., Köhler, P., Kudsk, S., Miyake, F., Olsen, J., Reinig, F., Sakamoto, M., Sookdeo, A., and Talamo, S.: The IntCal20 Northern Hemisphere Radiocarbon Age Calibration Curve (0–55 cal kBP), Radiocarbon, 62, 725–757, https://doi.org/10.1017/RDC.2020.41, 2020.

Renssen, H., Seppä, H., Crosta, X., Goosse, H., and Roche, D. M.: Global characterization of the Holocene thermal maximum,

840   Quaternary Science Reviews, 48, 7–19, https://doi.org/10.1016/j.quascirev.2012.05.022, 2012.

Robles, M., Peyron, O., Ménot, G., Brugiapaglia, E., Wulf, S., Appelt, O., Blache, M., Vannière, B., Dugerdil, L., Paura, B., Ansanay-Alex, S., Cromartie, A., Charlet, L., Guédron, S., de Beaulieu, J.-L., and Joannin, S.: Climate changes during the Lateglacial in South Europe: new insights based on pollen and brGDGTs of Lake Matese in Italy, Continental Surface Processes/Terrestrial Archives/Pleistocene, https://doi.org/10.5194/cp-2022-54, 2022a.

845   Robles, M., Peyron, O., Brugiapaglia, E., Ménot, G., Dugerdil, L., Ollivier, V., Ansanay-Alex, S., Develle, A.-L., Tozalakyan, P., Meliksetian, K., Sahakyan, K., Sahakyan, L., Perello, B., Badalyan, R., Colombié, C., and Joannin, S.: Impact of climate

changes on vegetation and human societies during the Holocene in the South Caucasus (Vanevan, Armenia): A multiproxy approach including pollen, NPPs and brGDGTs, Quaternary Science Reviews, 277, 107297, https://doi.org/10.1016/j.quascirev.2021.107297, 2022b.

850 Rodrigo-Gámiz, M., García-Alix, A., Jiménez-Moreno, G., Ramos-Román, M. J., Camuera, J., Toney, J. L., Sachse, D., Anderson, R. S., and Sinninghe Damsté, J. S.: Palaeoclimate reconstruction of the last 36 kyr based on branched glycerol dialkyl glycerol tetraethers in the Padul palaeolake record (Sierra Nevada, southern Iberian Peninsula), Quaternary Science Reviews, 281, 107434, https://doi.org/10.1016/j.quascirev.2022.107434, 2022.

Russell, J. M., Hopmans, E. C., Loomis, S. E., Liang, J., and Sinninghe Damsté, J. S.: Distributions of 5- and 6-methyl branched

855 glycerol dialkyl glycerol tetraethers (brGDGTs) in East African lake sediment: Effects of temperature, pH, and new lacustrine palaeotemperature calibrations, Organic Geochemistry, 117, 56–69, https://doi.org/10.1016/j.orggeochem.2017.12.003, 2018.

RStudio Team.: RStudio: Integrated Development for R, RStudio, PBC, Boston, MA burl, 2020.

Salonen, J. S., Korpela, M., Williams, J. W., and Luoto, M.: Machine-learning based reconstructions of primary and secondary climate variables from North American and European fossil pollen data, Sci Rep, 9, 15805, https://doi.org/10.1038/s41598-

860 019-52293-4, 2019.

Samartin, S., Heiri, O., Joos, F., Renssen, H., Franke, J., Brönnimann, S., and Tinner, W.: Warm Mediterranean mid-Holocene summers inferred from fossil midge assemblages, Nature Geosci, 10, 207–212, https://doi.org/10.1038/ngeo2891, 2017.

Schouten, S., Hopmans, E. C., Pancost, R. D., and Damsté, J. S. S.: Widespread occurrence of structurally diverse tetraether membrane lipids: Evidence for the ubiquitous presence of low-temperature relatives of hyperthermophiles, Proceedings of the

865 National Academy of Sciences, 97, 14421–14426, https://doi.org/10.1073/pnas.97.26.14421, 2000.

Schouten, S., Rijpstra, W. I. C., Durisch-Kaiser, E., Schubert, C. J., and Sinninghe Damsté, J. S.: Distribution of glycerol dialkyl glycerol tetraether lipids in the water column of Lake Tanganyika, Organic Geochemistry, 53, 34–37, https://doi.org/10.1016/j.orggeochem.2012.01.009, 2012.

Seppä, H. and Bennett, K. D.: Quaternary pollen analysis: recent progress in palaeoecology and palaeoclimatology, Progress

870 in Physical. Geography, 27, 548–579, 2003.

Silva-Sánchez, N., Martínez Cortizas, A., and López-Merino, L.: Linking forest cover, soil erosion and mire hydrology to late-Holocene human activity and climate in NW Spain, The Holocene, 24, 714–725, https://doi.org/10.1177/0959683614526934, 2014.

Sinninghe Damsté, J. S.: Spatial heterogeneity of sources of branched tetraethers in shelf systems: The geochemistry of

875 tetraethers in the Berau River delta (Kalimantan, Indonesia), Geochimica et Cosmochimica Acta, 186, 13–31, https://doi.org/10.1016/j.gca.2016.04.033, 2016.

Smith, A. C., Wynn, P. M., Barker, P. A., Leng, M. J., Noble, S. R., and Tych, W.: North Atlantic forcing of moisture delivery to Europe throughout the Holocene, Sci Rep, 6, 24745, https://doi.org/10.1038/srep24745, 2016.

Sugita, S., Parshall, T., Calcote, R.: Detecting differences in vegetation among paired sites using pollen records, The Holocene,

880 16, 1123-1135, 2006.

Sun, Q., Chu, G., Liu, M., Xie, M., Li, S., Ling, Y., Wang, X., Shi, L., Jia, G., and Lü, H.: Distributions and temperature dependence of branched glycerol dialkyl glycerol tetraethers in recent lacustrine sediments from China and Nepal, Journal of Geophysical. Research: Biogeosciences, 116, https://doi.org/10.1029/2010JG001365, 2011.

ter Braak, C. J. F. and Juggins, S.: Weighted averaging partial least squares regression (WA-PLS): an improved method for
885   reconstructing environmental variables from species assemblages | SpringerLink, Hydrobiologia, 269/270, 485–502, 1993.

Turner, M. G., Wei, D., Prentice, I. C., and Harrison, S. P.: The impact of methodological decisions on climate reconstructions using WA-PLS, Quaternary Research, 99, 341–356, https://doi.org/10.1017/qua.2020.44, 2021.

Wanner, H.: Late-Holocene: Cooler or warmer?, The Holocene, 31, 1501–1506, https://doi.org/10.1177/09596836211019106, 2021.

890   Weijers, J. W. H., Schouten, S., Linden, M., Geel, B., and Sinninghe Damsté, J. S.: Water table related variations in the abundance of intact archaeal membrane lipids in a Swedish peat bog, FEMS Microbiology Letters, 239, 51–56, https://doi.org/10.1016/j.femsle.2004.08.012, 2004.

Weijers, J. W. H., Schouten, S., Spaargaren, O. C., and Sinninghe Damsté, J. S.: Occurrence and distribution of tetraether membrane lipids in soils: Implications for the use of the TEX86 proxy and the BIT index, Organic Geochemistry, 37, 1680–
895   1693, https://doi.org/10.1016/j.orggeochem.2006.07.018, 2006.

Weijers, J. W. H., Schouten, S., van den Donker, J. C., Hopmans, E. C., and Sinninghe Damsté, J. S.: Environmental controls on bacterial tetraether membrane lipid distribution in soils, Geochimica et Cosmochimica Acta, 71, 703–713, https://doi.org/10.1016/j.gca.2006.10.003, 2007.

Weijers, J. W. H., Panoto, E., van Bleijswijk, J., Schouten, S., Rijpstra, W. I. C., Balk, M., Stams, A. J. M., and Damsté, J. S.
900   S.: Constraints on the Biological. Source(s) of the Or- phan Branched Tetraether Membrane Lipids, Geomicrobiology Journal, 26, 402–414, https://doi.org/10.1080/01490450902937293, 2009.

Wickham, H.: Data Analysis, in: ggplot2: Elegant Graphics for Data Analysis, edited by: Wickham, H., Springer International Publishing, Cham, 189–201, https://doi.org/10.1007/978-3-319-24277-4_9, 2016.

Xiong, Q., Pan, K., Zhang, L., Wang, Y., Li, W., He, X., and Luo, H.: Warming and nitrogen deposition are interactive in
905   shaping surface soil microbial communities near the alpine timberline zone on the eastern Qinghai–Tibet Plateau, southwestern China, Applied Soil Ecology, 101, 72–83, https://doi.org/10.1016/j.apsoil.2016.01.011, 2016.

Yang, H., Pancost, R. D., Dang, X., Zhou, X., Evershed, R. P., Xiao, G., Tang, C., Gao, L., Guo, Z., and Xie, S.: Correlations between microbial tetraether lipids and environmental variables in Chinese soils: Optimizing the palaeo-reconstructions in semi-arid and arid regions, Geochimica et Cosmochimica Acta, 126, 49–69, https://doi.org/10.1016/j.gca.2013.10.041, 2014.

910   Yang, H., Xiao, W., Słowakiewicz, M., Ding, W., Ayari, A., Dang, X., and Pei, H.: Depth-dependent variation of archaeal ether lipids along soil and peat profiles from southern China: Implications for the use of isoprenoidal GDGTs as environmental tracers, Organic Geochemistry, 128, 42–56, https://doi.org/10.1016/j.orggeochem.2018.12.009, 2019.

Yurtsev, B.A.: Relics of the xerophyte vegetation of Beringia in northeastern Asia, in: Paleoecology of Beringia, edited by: Hopkins, D.M., Matthews Jr., J.V., Schweger, C.E., and Young, S.B., Academic Press, New York, 157–177, 1982.

915   Zheng, Y., Li, Q., Wang, Z., Naafs, B. D. A., Yu, X., and Pancost, R. D.: Peatland GDGT re- cords of Holocene climatic and biogeochemical. responses to the Asian Monsoon, Organic Geochemistry, 87, 86–95, https://doi.org/10.1016/j.orggeochem.2015.07.012, 2015.